Multi-hp adaptive discontinuous Galerkin methods for simplified P_N approximations of 3D radiative transfer in non-gray media

Stefano Giani* Mohammed Seaid†

Abstract

In this paper we present a multi-hp adaptive discontinuous Galerkin method for 3D simplified P_N approximations of radiative transfer in non-gray media capable of reaching accuracies superior to most of methods in the literature. The simplified P_N models are a set of differential equations derived based on asymptotic expansions for the integro-differential radiative transfer equation. In a non-gray media the optical spectrum is divided into a finite set of bands with constant absorption coefficients and the simplified P_N approximations are solved for each band in the spectrum. At high temperature, boundary layers with different magnitudes occur for each wavelength in the spectrum and developing a numerical solver to accurately capture them is challenging for the conventional finite element methods. Here we propose a class of high-order adaptive discontinuous Galerkin methods using space error estimators. The proposed method is able to solve problems where 3D meshes contain finite elements of different kind with the number of equations and polynomial orders of approximation varying locally on the finite element edges, faces, and interiors. The proposed method has also the potential to perform both isotropic and anisotropic adaptation for each band in the optical spectrum. Several numerical results are presented to illustrate the performance of the proposed method for 3D radiative simulations. The computed results confirm its capability to solve 3D simplified P_N approximations of radiative transfer in non-gray media.

Keywords. Radiative transfer problems; Simplified P_N approximations; Discontinuous Galerkin method; *hp*-adaptivity; Error estimators

1 Introduction

Modelling and simulation of radiative transfer are for decades a vast research area in mathematics and engineering, see [24, 1, 2] and the references therein. The main focus in these studies is on the analytical and numerical resolutions of the boundary layers due to temperature gradients. At high temperatures, radiative transfer is a key in many Engineering applications such as glass melting furnaces, design of combustion chambers for gas turbines, or crystal growth processes [5, 8, 26]. In the full simulation of thermal radiation, the integro-differential equation for the radiative transfer needs to be solved in conjunction with the partial differential equations governing momentum, energy transport and chemical reactions [17]. The zonal and Monte Carlo methods have been widely considered in the literature as the most accurate numerical solvers for radiative transfer, see for example [18]. However, these methods suffer from high computational times and storage

*School of Engineering, University of Durham, South Road, Durham DH1 3LE, UK *E-mail:* stefano.giani@durham.ac.uk

†School of Engineering, University of Durham, South Road, Durham DH1 3LE, UK *E-mail:* m.seaid@durham.ac.uk

requirements. In addition, these techniques are suitable for integro-differential equations but not for partial differential equations governing heat conduction, flow convection, and combustion, see for instance [19, 17, 25]. The discrete ordinate methods [7] appear to be reasonable compromises for solving the radiative transfer equations, but still one has to deal with large systems of algebraic equations associated with the discretization of the frequency, the angle and the space variables which are detrimental to the efficiency of solving coupled radiative heat transfer and flow, see [22, 21] and further references are therein.

Nowadays, there is a strong need either for appropriate fast and accurate algorithms for the radiative transfer or for reduced models which still incorporate its main radiative transfer physics [23, 21]. During the last decade, a lot of research was focused on the derivation of approximate models allowing for an accurate description of the important physical phenomena at reasonable numerical costs. Hence, a whole hierarchy of approximative equations is available, ranging from half-space moment approximations over full-space moment systems to the diffusion-type simplified P_N (SP_N) approximations, see for example [16, 15]. The latter were developed and extensively tested for various radiative transfer problems, where they proved to be sufficiently accurate [21]. Although they were derived in the asymptotic regime for a large optical thickness of the material, these approximations yield encouraging even results in the optically thin regime. The main advantage of considering simplified P_N approximations is the fact that the integro-differential radiative transfer equation is transformed into a set of elliptic equations independent of the angular direction which are easy to solve. Furthermore, comparisons presented in [5, 15, 8, 23, 21] among others have demonstrated that in optically thick media the simplified P_N models approximate the numerical solutions of the full radiative heat transfer problem with a very low computational cost.

In the current study, Discontinuous Galerkin (DG) methods [4] are our solvers of choice because the discontinuities across faces make them ideal methods to be used with anisotropic adaptivity. After the first analysis of DG methods on anisotropic meshes [9, 10], further refinements have been followed. In view of this work, the analysis presented in [20, 27, 11] is fundamental for the derivation of the error estimator for the simplified P_N approximations and for the reliability of it. This study differs from our previous work [12] in many ways and not only because it focuses on 3D problems. The error estimator presented in this paper is new since the error estimator analysis is not independent of the number of dimensions, compare the definition of $\eta_{J,K}$ in [12] and in Section 3, and also because in this work we consider anisotropic order of polynomials for the elements which also affect the definition of the error estimator. In particular, the exact form of the error estimator

the coefficients involving h and p for the face terms are different and specific for the 3D case. The correctness of these coefficients is what ensures the efficiency of the error estimator, *i.e.* the ability of the error estimator to mimic the behavior of the true error. In addition, the error estimator analysis has been improved to exploit anisotropic adaptivity in the order of polynomials. This feature allows for different polynomial orders in different directions within an element and therefore, makes the method more efficient and robust. Finally, a new refinement strategy to take advantage of the new capabilities of the error estimator is presented in this study compared to our previous work for 2D problems in [12]. This is the anisotropic *hp*-refinement procedure which applies anisotropic refinement in both h and p. This procedure is particularly interesting in the 3D case where the number of degrees of freedom increases very rapidly with p due to the number of dimensions. For this technique, increasing the order of polynomials independently in each direction, ensures a more economical usage of the degrees of freedom. To examine the performance of the proposed techniques we solve a wide range of examples for 3D radiative transfer problems in both gray and non-gray media. The multi-hp adaptive DG method is also used to solve the SP_N approximations of a radiative transfer involving the CO_2 species at high temperature using an optical spectrum with 67 bands.

The paper is organized as follows. In section 2 we formulate the $\mathrm{SP_N}$ approximations where we will especially introduce the $\mathrm{SP_1}$ and the $\mathrm{SP_3}$ systems. The multi-hp adaptive discontinuous Galerkin method is presented in section 3. This section includes the discontinuous Galerkin discretization and the *hp*-error estimators for the $\mathrm{SP_N}$ equations. Numerical results and comparisons using several test examples in radiative transfer are discussed in section 4. Finally, conclusions are given in section 5.

2 Simplified $\mathrm{P_N}$ approximations of radiative transfer

In this study we assume a three-dimensional domain Ω with a boundary $\partial\Omega$ of an emitting and absorbing semitransparent material subject to a prescribed temperature distribution T inside Ω and a given surrounding temperature T_b on $\partial\Omega$. Hence, the spectral radiative intensity $I(\mathbf{x},\mathbf{s},\nu)$ along the direction $\mathbf{s}$, at the space point $\mathbf{x}$ and within the frequency ν is obtained from the dimensionless radiative transfer equation

$$\epsilon\mathbf{s}\cdot\nabla I+(\kappa+\sigma)\,I=\frac{\sigma}{4\pi}\int_{S^2}I(\mathbf{x},\mathbf{s}',\nu)d\mathbf{s}'+\kappa B(T,\nu,n_{\mathrm{m}}),\quad(\mathbf{x},\mathbf{s},\nu)\in\Omega\times S^2\times]\nu_0,\infty),\tag{1}$$

where $\kappa(\nu)$ is the absorption coefficient, $\sigma(\nu)$ the scattering coefficient, ϵ the optical thickness coefficient and $B(T,\nu,n_{\mathrm{m}})$ the spectral intensity of the black-body radiation given by the Planck function in a medium with refractive index n_{m} as [17]

$$B(T,\nu,n_{\mathrm{m}})=\frac{2h_P\nu^3}{c_0^2}n_{\mathrm{m}}^2\big(e^{h_P\nu/k_BT}-1\big)^{-1},\tag{2}$$

where h_P, k_B and c_0 are Planck constant, Boltzmann constant and the speed of radiation propagation in the vacuum, respectively. Here, the integro-differential equation (1) models the changes of the radiative intensity $I(\mathbf{x},\mathbf{s},\nu)$ as particles are passing through the domain Ω at the position point $\mathbf{x}$ along the direction $\mathbf{s}$ in the unit sphere S^2 with the frequency ν. These particles are subject to losses due to the scattering σ and the absorption κ while their number grows due to the black-body radiation source $B(T,\nu,n_{\mathrm{m}})$ inside a medium with the refractive index n_{m}. On the boundary $\partial\Omega$ we consider the specular reflecting and transmitting conditions

$$I(\hat{\mathbf{x}},\mathbf{s},\nu)-\varrho(\mathbf{n}\cdot\mathbf{s})I(\hat{\mathbf{x}},\mathbf{s}',\nu)=\Big(1-\varrho(\mathbf{n}\cdot\mathbf{s})\Big)B(T_b,\nu,n_{\mathrm{b}}),\quad(\hat{\mathbf{x}},\mathbf{s},\nu)\in\partial\Omega^-\times S^2\times]\nu_0,\infty),\tag{3}$$

where

$$\partial\Omega^-=\Big\{\hat{\mathbf{x}}\in\partial\Omega;\quad\mathbf{n}(\hat{\mathbf{x}})\cdot\mathbf{s}<0\Big\},$$

with $\mathbf{n}(\hat{\mathbf{x}})$ is the outward normal at $\hat{\mathbf{x}}$ on $\partial\Omega$, $\mathbf{s}'=\mathbf{s}-2(\mathbf{n}\cdot\mathbf{s})\mathbf{n}$ is the specular reflection of $\mathbf{s}$ on $\partial\Omega$, and $\varrho\in[0,1]$ is the medium reflectivity obtained according to the Fresnel and Snell laws [26]. For an incident angle θ_{m} given by $\cos\theta_{\mathrm{m}}=|\mathbf{n}\cdot\mathbf{s}|$ and Snell's law

$$n_{\mathrm{b}}\sin\theta_{\mathrm{b}}=n_{\mathrm{m}}\sin\theta_{\mathrm{m}},$$

the reflectivity $\varrho(\mu)$, $\mu=|\mathbf{n}\cdot\mathbf{s}|$, is defined as

$$\varrho(\mu)=\begin{cases}\dfrac{1}{2}\left(\dfrac{\tan^2(\theta_{\mathrm{m}}-\theta_{\mathrm{b}})}{\tan^2(\theta_{\mathrm{m}}+\theta_{\mathrm{b}})}+\dfrac{\sin^2(\theta_{\mathrm{m}}-\theta_{\mathrm{b}})}{\sin^2(\theta_{\mathrm{m}}+\theta_{\mathrm{b}})}\right), & \text{if}\quad\Big|\sin\theta_{\mathrm{m}}\Big|\le\dfrac{n_{\mathrm{b}}}{n_{\mathrm{m}}},\\[2ex] 1, & \text{otherwise,}\end{cases}\tag{4}$$

where $n_{\rm b}$ is the refractive index of the surrounding medium. In the present work we divide the optical spectrum into a finite set of bands as

$$[0,\nu] = \bigcup_{k=1}^{N_\nu} [\nu_{k-1},\nu_k]\,,$$

with N_ν is the total number of spectral bands. We also assume that the spectral absorption $\kappa(\nu)$ and the scattering $\sigma(\nu)$ are piecewise constants with respect to the frequency ν, *i.e.*

$$\kappa(\nu) = \kappa_k, \qquad \sigma(\nu) = \sigma_k, \qquad \forall\ \nu \in [\nu_{k-1},\nu_k]\,, \quad k = 1,2,\ldots,N_\nu, \tag{5}$$

with κ_k and σ_k are constants in the band $[\nu_{k-1},\nu_k]$. For each optical band k, we define the local spectral intensity $I^{(k)}(\mathbf{x},\mathbf{s})$, the local mean intensity $\varphi^{(k)}(\mathbf{x})$ and the local Plankian function $B^{(k)}(T,n_{\rm m})$ as

$$I^{(k)}(\mathbf{x},\mathbf{s}) = \int_{\nu_k}^{\nu_{k+1}} I(\mathbf{x},\mathbf{s},\nu)d\nu,\ \varphi^{(k)}(\mathbf{x}) = \int_{S^2} I^{(k)}(\mathbf{x},\mathbf{s})d\mathbf{s},\ B^{(k)}(T,n_{\rm m}) = \int_{\nu_k}^{\nu_{k+1}} B(T,\nu,n_{\rm m})d\nu.$$

Hence, the radiative transfer equations (1) and (3) can be formulated as

$$\begin{aligned}
\varepsilon\mathbf{s}\cdot\nabla I^{(k)} + (\kappa_k+\sigma_k)\, I^{(k)} &= \frac{\sigma_k}{4\pi}\varphi^{(k)} + \kappa_k B^{(k)}(T,n_{\rm m}), &\text{(6a)}\\
I^{(k)}(\hat{\mathbf{x}},\mathbf{s}) - \varrho(\mathbf{n}\cdot\mathbf{s})I^{(k)}(\hat{\mathbf{x}},\mathbf{s}') &= \Big(1-\varrho(\mathbf{n}\cdot\mathbf{s})\Big)B^{(k)}(T_b,n_{\rm b}). &\text{(6b)}
\end{aligned}$$

It should be pointed out that more details on modelling radiative transfer in non-gray diffusive semitransparent media can be found in [18, 26] among others. Physical assumptions made to derive the governing equations (1) are also discussed in these references. In this section, we briefly present the $\mathrm{SP_N}$ approximations for the radiative transfer equations (6). For more analysis we refer the reader to [15] and further references are therein. Thus, we reformulate the equation (6a) as

$$\left(1+\frac{\varepsilon}{\kappa_k+\sigma_k}\mathbf{s}\cdot\nabla\right) I^{(k)} = \mathcal{Q}^{(k)},$$

where the source term $\mathcal{Q}^{(k)}$ is defined by

$$\mathcal{Q}^{(k)} = \frac{\sigma_k}{4\pi\,(\kappa_k+\sigma_k)}\varphi^{(k)} + \frac{\kappa_k}{\kappa_k+\sigma_k}B^{(k)}(T,n_{\rm m}).$$

Next we apply the Neumann series to formally invert the transport operator as

$$\begin{aligned}
I^{(k)} &= \left(1+\frac{\varepsilon}{\kappa_k+\sigma_k}\mathbf{s}\cdot\nabla\right)^{-1}\mathcal{Q}^{(k)},\\
&\approx \left(1-\frac{\varepsilon}{\kappa_k+\sigma_k}\mathbf{s}\cdot\nabla+\frac{\varepsilon^2}{(\kappa_k+\sigma_k)^2}(\mathbf{s}\cdot\nabla)^2-\frac{\varepsilon^3}{(\kappa_k+\sigma_k)^3}(\mathbf{s}\cdot\nabla)^3+\right.\\
&\quad \left.\frac{\varepsilon^4}{(\kappa_k+\sigma_k)^4}(\mathbf{s}\cdot\nabla)^4-\frac{\varepsilon^5}{(\kappa_k+\sigma_k)^5}(\mathbf{s}\cdot\nabla)^5+\cdots\right)\mathcal{Q}^{(k)}. \qquad (7)
\end{aligned}$$

We then integrate the expansion (7) with respect to $\mathbf{s}$ over all directions in the unit sphere S^2 and we use the well-established relation

$$\int_{S^2}\big(\mathbf{s}\cdot\nabla\big)^n d\mathbf{s} = \Big(1+(-1)^n\Big)\frac{2\pi}{n+1}\nabla^n.$$

Hence, the formal asymptotic equation for $\varphi^{(k)}$ is given by

$$4\pi\mathcal{Q}^{(k)} = \left(1 - \frac{\varepsilon^2}{3\left(\kappa_k+\sigma_k\right)^2}\nabla^2 - \frac{4\varepsilon^4}{45\left(\kappa_k+\sigma_k\right)^4}\nabla^4 - \frac{44\varepsilon^6}{94\left(\kappa_k+\sigma_k\right)^6}\nabla^6\right)\varphi^{(k)} + \mathcal{O}(\varepsilon^8).$$

By neglecting the terms of order $\mathcal{O}(\varepsilon^2)$, $\mathcal{O}(\varepsilon^4)$, $\mathcal{O}(\varepsilon^6)$ or $\mathcal{O}(\varepsilon^8)$ one obtains the SP_0, SP_1, SP_2 or SP_3 approximations, respectively. Note that higher order approximations can also be derived in the same manner. Here, we consider only the SP_1 and SP_3 approximations but our DG method can easily be extended to other approximations. The boundary conditions for the SP_N approximations are obtained from variational principles and are closely related to the Marshak conditions for the P_N approximations, see for example [18]. In what follows, we briefly state the set of equations for the SP_1 and SP_3 approximations and more details can be found in [15]. For the SP_1 approximation:

$$4\pi\mathcal{Q}^{(k)} = \varphi^{(k)} - \frac{\varepsilon^2}{3\left(\kappa_k+\sigma_k\right)^2}\nabla^2\varphi^{(k)} + \mathcal{O}(\varepsilon^4),$$

and the SP_1 model reads

$$\begin{aligned} -\nabla\cdot\left(\frac{\varepsilon^2}{3\left(\kappa_k+\sigma_k\right)}\nabla\varphi^{(k)}\right) + \kappa_k\varphi^{(k)} &= 4\pi\kappa_k B^{(k)}(T, n_\mathrm{m}), \\ \varphi^{(k)} + \left(\frac{1+3r_2}{1-2r_1}\frac{2\varepsilon}{3\left(\kappa_k+\sigma_k\right)}\right)\mathbf{n}(\hat{\mathbf{x}})\cdot\nabla\varphi^{(k)} &= 4\pi B^{(k)}(T_b, n_\mathrm{b}). \end{aligned} \tag{8}$$

The parameters r_1 and r_2 appearing in the boundary conditions for $\varphi^{(k)}$ depend on reflectivity of the considered media $\varrho(\mu)$ in (4) and their formulations are given below. For the SP_3 approximation:

$$4\pi\mathcal{Q}^{(k)} = \left(1 - \frac{\varepsilon^2}{3\left(\kappa_k+\sigma_k\right)^2}\nabla^2 - \frac{4\varepsilon^4}{45\left(\kappa_k+\sigma_k\right)^4}\nabla^4 - \frac{44\varepsilon^6}{94\left(\kappa_k+\sigma_k\right)^6}\nabla^6\right)\varphi^{(k)} + \mathcal{O}(\varepsilon^8),$$

and the SP_3 model is defined as [15]

$$\begin{aligned} -\nabla\cdot\left(\frac{\varepsilon^2\mu_1^2}{\kappa_k+\sigma_k}\nabla\psi_1^{(k)}\right) + \kappa_k\psi_1^{(k)} &= 4\pi\kappa_k B^{(k)}(T, n_\mathrm{m}), \\ -\nabla\cdot\left(\frac{\varepsilon^2\mu_2^2}{\kappa_k+\sigma_k}\nabla\psi_2^{(k)}\right) + \kappa_k\psi_2^{(k)} &= 4\pi\kappa_k B^{(k)}(T, n_\mathrm{m}), \\ \alpha_1\psi_1 + \frac{\varepsilon}{\kappa_k+\sigma_k}\mathbf{n}(\hat{\mathbf{x}})\cdot\nabla\psi_1^{(k)} &= -\beta_2\psi_2^{(k)} + \eta_1 B^{(k)}(T_b, n_\mathrm{b}), \\ \alpha_2\psi_2 + \frac{\varepsilon}{\kappa_k+\sigma_k}\mathbf{n}(\hat{\mathbf{x}})\cdot\nabla\psi_2^{(k)} &= -\beta_1\psi_1^{(k)} + \eta_2 B^{(k)}(T_b, n_\mathrm{b}). \end{aligned} \tag{9}$$

The mean radiative intensity $\varphi^{(k)}$ is calculated from the variables $\psi_1^{(k)}$ and $\psi_2^{(k)}$ as

$$\varphi^{(k)} = \frac{\gamma_2\psi_1^{(k)} - \gamma_1\psi_2^{(k)}}{\gamma_2 - \gamma_1}, \qquad k = 1, 2, \ldots, N_\nu.$$

Next we briefly summarize the parameters required in the boundary conditions for the SP_N approximations (8) and (9). For more details on the asymptotic analysis used to derive these conditions we refer the reader to [15]. Hence, we define the integrals r_i $(i = 1, \ldots 7)$ by

$$r_1 = \int_0^1 \mu\varrho(-\mu)d\mu, \quad r_3 = \int_0^1 \mu^3\varrho(-\mu)d\mu, \qquad r_6 = \int_0^1 P_1(\mu)P_3(\mu)\varrho(-\mu)d\mu,$$

$$r_2 = \int_0^1 \mu^2\varrho(-\mu)d\mu, \quad r_4 = \int_0^1 \mu P_3(\mu)\varrho(-\mu)d\mu, \quad r_5 = \int_0^1 P_3(\mu)\varrho(-\mu)d\mu,$$

$$r_7 = \int_0^1 P_3(\mu) P_3(\mu) \varrho(-\mu) d\mu,$$

where ϱ is the reflectivity of the medium given in (4), P_1 and P_3 are the first-order and third-order Legendre polynomials defined as

$$P_1(\mu) = \mu, \qquad P_3(\mu) = \frac{5}{2}\mu^3 - \frac{3}{2}\mu.$$

The constants appearing in the boundary condition of the SP_3 approximation (9) are

$$\mu_1^2 = \frac{1}{7}\left(3 - 2\sqrt{\frac{6}{5}}\right), \quad \gamma_1 = \frac{5}{7}\left(1 - 3\sqrt{\frac{6}{5}}\right), \quad \mu_2^2 = \frac{1}{7}\left(3 + 2\sqrt{\frac{6}{5}}\right), \quad \gamma_2 = \frac{5}{7}\left(1 + 3\sqrt{\frac{6}{5}}\right),$$

$$\begin{aligned}
\alpha_1 &= \frac{C_1 D_4 - C_4 D_1}{C_3 D_4 - D_3 C_4}, \qquad \beta_1 = \frac{C_3 D_1 - C_1 D_3}{C_3 D_4 - D_3 C_4}, \qquad \eta_1 = \frac{D_4 \rho_1 - C_4 \rho_3}{C_3 D_4 - D_3 C_4}, \\
\alpha_2 &= \frac{C_3 D_2 - C_2 D_3}{C_3 D_4 - D_3 C_4}, \qquad \beta_2 = \frac{C_2 D_4 - C_4 D_2}{C_3 D_4 - D_3 C_4}, \qquad \eta_2 = \frac{C_3 \rho_3 - D_3 \rho_1}{C_3 D_4 - D_3 C_4},
\end{aligned}$$

where

$$\begin{aligned}
A_1 &= \frac{1 - 2r_1}{4}, & B_1 &= -\frac{1 + 8r_5}{16}, & C_1 &= w_0(\gamma_2 A_1 - A_2), & D_1 &= w_0(\gamma_2 B_1 - B_2), \\
A_2 &= \frac{5(1 - 8r_3)}{16}, & B_2 &= \frac{5(1 - 8r_6)}{16}, & C_2 &= w_0(-\gamma_1 A_1 + A_2), & D_2 &= w_0(-\gamma_1 B_1 + B_2), \\
A_3 &= \frac{1 + 3r_2}{6}, & B_3 &= \frac{3r_4}{6}, & C_3 &= w_0(\gamma_2 A_3 - A_4), & D_3 &= w_0(\gamma_2 B_3 - B_4),
\end{aligned}$$

$$A_4 = r_4 + \frac{2(1 + 3r_2)}{9}, \; B_4 = r_4 + \frac{3(1 + 7r_7)}{14}, \; C_4 = w_0(-\gamma_1 A_3 - A_4), \; D_4 = w_0(-\gamma_1 B_3 + B_4),$$

with

$$w_0 = \frac{7}{36}\sqrt{\frac{6}{5}}, \qquad \rho_1 = (1 - 2r_1)\,\pi, \qquad \rho_3 = -\left(\frac{1}{4} + 2r_5\right)\pi.$$

It is worth noting that these parameters depend only on the optical reflectivity of the media considered for the radiative transfer. In our simulations, these parameters are calculated in advance and stored to be used whenever a simulation of solution has to be repeated in the frequency loop.

3 The hp-adaptive discontinuous Galerkin method

In this section we formulate our DG method for solving the SP_1 and SP_3 approximations given by the systems (8) and (9), respectively. We also describe the error estimators used for the *hp*-adaptivity procedures. For simplicity in the presentation, the SP_1 and SP_3 approximations are rearranged in a compact form as

$$\begin{aligned}
-\nabla \cdot (\mathcal{A} \nabla \phi) + \mathcal{B}\phi &= \mathcal{F}, \\
\mathcal{C}\mathbf{n}(\hat{\mathbf{x}}) \cdot \nabla \phi + \mathcal{D}\phi &= \mathcal{G}.
\end{aligned} \tag{10}$$

For the SP_1 approximation

$$\phi = \varphi, \quad \mathcal{A} = \frac{\varepsilon^2}{3\,(\kappa_k + \sigma_k)}, \qquad \mathcal{B} = \kappa_k, \qquad \mathcal{C} = \frac{1 + 3r_2}{1 - 2r_1}\frac{2\varepsilon}{3\,(\kappa_k + \sigma_k)}, \qquad \mathcal{D} = 1,$$

$$\mathcal{F} = 4\pi\kappa_k B^{(k)}(T, n_{\rm m}), \qquad \mathcal{G} = 4\pi B^{(k)}(T_b, n_{\rm b}).$$

For the SP_3 approximation

$$\phi = \begin{pmatrix} \psi_1 \\ \\ \psi_2 \end{pmatrix}, \quad \mathcal{A} = \begin{pmatrix} \dfrac{\varepsilon^2\mu_1^2}{\kappa_k+\sigma_k} & 0 \\ 0 & \dfrac{\varepsilon^2\mu_2^2}{\kappa_k+\sigma_k} \end{pmatrix}, \quad \mathcal{B} = \begin{pmatrix} \kappa_k \\ \\ \kappa_k \end{pmatrix}, \quad \mathcal{C} = \begin{pmatrix} \dfrac{\varepsilon}{\kappa_k+\sigma_k} \\ \\ \dfrac{\varepsilon}{\kappa_k+\sigma_k} \end{pmatrix},$$

$$\mathcal{D} = \begin{pmatrix} \alpha_1 & \beta_2 \\ \\ \beta_1 & \alpha_2 \end{pmatrix}, \qquad \mathcal{F} = \begin{pmatrix} 4\pi\kappa_k B^{(k)}(T, n_{\rm m}) \\ \\ 4\pi\kappa_k B^{(k)}(T, n_{\rm m}) \end{pmatrix}, \qquad \mathcal{G} = \begin{pmatrix} \eta_1 B^{(k)}(T_b, n_{\rm b}) \\ \\ \eta_2 B^{(k)}(T_b, n_{\rm b}) \end{pmatrix}.$$

Note that differently from other methods in the literature [5, 15, 8, 23, 21], we solve the SP_3 system monolithically instead of decoupling the equations and solving them separately.

In the present work, all the meshes ζ are discretizations of the space domain Ω and they are assumed to be shape-regular with at most one hanging node per edge and at most one hanging node per face. Furthermore, we denote by K the generic hexahedral element in ζ. We assume everywhere in the paper that the subdivision ζ is constructed via affine mappings $F_K : \hat{K} \longrightarrow K$ with non-singular Jacobian where $\hat{K}$ is the reference cube. We also use the notation $\mathcal{F}(\zeta)$ and $\mathcal{F}^{int}(\zeta) \subset \mathcal{F}(\zeta)$ to denote the set of all faces in the mesh ζ and the subset of all interior faces and by $\mathcal{F}^{BC}(\zeta) \subset \mathcal{F}(\zeta)$ the subset of all boundary faces, respectively. To describe anisotropic elements, we define the following quantities for each hexahedral element $K \in \zeta$, we define the three vectors $\underline{\mathrm{v}}_K^1$, $\underline{\mathrm{v}}_K^2$ and $\underline{\mathrm{v}}_K^3$ pairwise orthogonal and oriented as the axes of the element K. These vectors reflect the three anisotropic directions of the generic element K and their lengths are denoted by h_K^1, h_K^2 and h_K^3, respectively. Thus,

$$h_K^1 = \text{length}\left(\underline{\mathrm{v}}_K^1\right), \qquad h_K^2 = \text{length}\left(\underline{\mathrm{v}}_K^2\right), \qquad h_K^3 = \text{length}\left(\underline{\mathrm{v}}_K^3\right).$$

We also set

$$h_{\min,K} = \min\left(h_K^1, h_K^2, h_K^3\right), \qquad h_{\max,K} = \max\left(h_K^1, h_K^2, h_K^3\right).$$

Let $\mathbf{M}_K$ denote the matrix formed by the anisotropic vectors $\underline{\mathrm{v}}_K^1$, $\underline{\mathrm{v}}_K^2$ and $\underline{\mathrm{v}}_K^3$ as

$$\mathbf{M}_K = \left(\underline{\mathrm{v}}_K^1, \underline{\mathrm{v}}_K^2, \underline{\mathrm{v}}_K^3\right).$$

Note that the matrix $\mathbf{M}_K$ is orthogonal and it satisfies

$$\mathbf{M}_K^\top \mathbf{M}_K = \begin{pmatrix} (h_K^1)^2 & 0 & 0 \\ 0 & (h_K^2)^2 & 0 \\ 0 & 0 & (h_K^3)^2 \end{pmatrix}.$$

Given a face $F \in \mathcal{F}(\zeta)$, for any element $K \in \zeta$, if $F \in \mathcal{F}(K)$ then F is a part of an elemental face of K. We define a local function $\mathrm{h}_{F,K}^\perp$ of the face F as the h_K^i along the direction perpendicular to the face F. Moreover, for any $F \in \mathcal{F}^{int}(\zeta)$, we assume that

$$\mathrm{h}_{F,K}^\perp \sim \mathrm{h}_{F,K'}^\perp, \qquad F = K \cap K', \quad K, K' \in \zeta. \tag{11}$$

Notice that the assumption (11) does not bound the aspect ratios of elements. For any face $F \in \mathcal{F}(\zeta)$, we further set

$$\mathrm{h}_F^\perp = \begin{cases} \min\left(\mathrm{h}_{F,K}^\perp, \mathrm{h}_{F,K'}^\perp\right), & \text{if} \quad F \in \mathcal{F}^{int}(\zeta), \quad F = \partial K \cap \partial K', \\ \\ \mathrm{h}_{F,K}^\perp, & \text{if} \quad F \in \mathcal{F}(\zeta) \setminus \mathcal{F}^{int}(\zeta), \quad F = \partial K \cap \partial\Omega. \end{cases}$$

We then define $h_{\min,F}$ by

$$h_{\min,F} = \begin{cases} \min\left(h_{\min,K},\, h_{\min,K'}\right), & \text{if} \quad F \in \mathcal{F}^{int}(\zeta), \quad F = \partial K \cap \partial K', \\ \\ h_{\min,K}, & \text{if} \quad F \in \mathcal{F}(\zeta) \setminus \mathcal{F}^{int}(\zeta), \quad F = \partial K \cap \partial\Omega, \end{cases}$$

Next we introduce the polynomial degrees for the approximation in our DG method. On each element K the anisotropic polynomial space is described by a triplet $\underline{p}_K := \{p_K^i\}_{i=1,2,3}$ containing the order of polynomials in each direction. We then define

$$p_{\min,K} := \min_{i=1,2,3}\{p_K^i\}\ , \quad p_{\max,K} := \max_{i=1,2,3}\{p_K^i\}\ , \quad p_{\max} := \max_{K\in\zeta}\{p_{max,K}\},$$

For a face $F \in \mathcal{F}(\zeta)$, we define $p_{F,K} := \max\{p_K^i, p_K^j\}$ with F parallel to $\underline{\mathrm{v}}_K^i$ and $\underline{\mathrm{v}}_K^j$, $i,j = 1,2,3$, $i \neq j$, and $p_{F,K}^{\perp} := p_K^i$ if F is perpendicular to the direction i, for $i = 1,2,3$. We assume that $\underline{p}$ is of bounded local variation such that, for any $F \in \mathcal{F}^{int}(\zeta)$, we have

$$p_{F,K}^{\perp} \sim p_{F,K'}^{\perp}\ , \quad p_{F,K} \sim p_{F,K'},$$

where K and K' share the same face F. Then, for any edge $F \in \mathcal{F}(\zeta)$, we also introduce the notations:

$$p_F^{\perp} = \begin{cases} \max\{p_{F,K}^{\perp}, p_{F,K'}^{\perp}\}, & \text{if} F = \partial K \cap \partial K' \in \mathcal{F}^{int}(\zeta), \\ \\ p_{F,K}^{\perp}, & \text{if } F = \partial K \cap \partial\Omega \in \mathcal{F}(\zeta) \setminus \mathcal{F}^{int}(\zeta), \end{cases}$$

$$p_{\max,F} = \begin{cases} \max\{p_{\max,K}, p_{\max,K'}\}, & \text{if} F = \partial K \cap \partial K' \in \mathcal{F}^{int}(\zeta), \\ \\ p_{\max,K}, & \text{if } F = \partial K \cap \partial\Omega \in \mathcal{F}(\zeta) \setminus \mathcal{F}^{int}(\zeta). \end{cases}$$

Let $\mathbf{n}_K$ denotes the outward unit normal on the boundary ∂K of an element K. Given a face $F \in \mathcal{F}^{int}(\zeta)$ shared by two elements K^+ and K^-, we define the jumps and the averages of a vector field $\mathbf{v}$ and of a scalar field v across F by

$$\{v\} = \frac{1}{2}\left(v\Big|_{\bar{K}^+} + v\Big|_{\bar{K}^-}\right), \qquad [v] = v\Big|_{\bar{K}^+}\mathbf{n}_K + v\Big|_{\bar{K}^-}\mathbf{n}_{K'},$$

$$\{\mathcal{A}\mathbf{v}\} = \frac{1}{2}\left(\mathcal{A}\mathbf{v}\Big|_{\bar{K}^+} + \mathcal{A}\mathbf{v}\Big|_{\bar{K}^-}\right), \qquad [\mathcal{A}\mathbf{v}] = \mathcal{A}\mathbf{v}\Big|_{\bar{K}^+}\cdot\mathbf{n}_K + \mathcal{A}\mathbf{v}\Big|_{\bar{K}^-}\cdot\mathbf{n}_{K'}.$$

Note that if $F \subset \partial\Omega$, we set $\{\mathbf{v}\} = \mathbf{v}$, $[\mathbf{v}] = \mathbf{v}\cdot\mathbf{n}$, $\{v\} = v$ and $[v] = v\mathbf{n}$, with $\mathbf{n}$ is the outward unit normal to the boundary $\partial\Omega$.

The derivation of the DG method for solving SP_1 and SP_3 equations can be performed using similar techniques as those reported in [4]. Thus, the DG approximation for the SP_1 problem reads as follows: Find $\phi_h \in V_{\mathbf{p}}(\zeta)$ such that

$$B\left(\phi_h, v_h\right) + K_h\left(\phi_h, v_h\right) = \left(\mathcal{F}, v_h\right) + \sum_{F\in\mathcal{F}^{BC}(\zeta)}\int_F \frac{\mathcal{A}}{\mathcal{C}}\mathcal{G}v_h\, ds, \qquad \forall v_h \in V_{\mathbf{p}}(\zeta)\ ,$$

where the bilinear forms

$$\begin{aligned} B\left(w,v\right) &= \sum_{K\in\zeta}\int_K\left(\mathcal{A}\nabla w\cdot\nabla v + \mathcal{B}wv\right)d\mathbf{x} + \sum_{F\in\mathcal{F}^{int}(\zeta)}\frac{\gamma\mathcal{A}(p_F^{\perp})^2}{h_F^{\perp}}\int_F [w]\cdot[v]\, ds, \\ K_h\left(w,v\right) &= -\sum_{F\in\mathcal{F}^{int}(\zeta)}\int_F \{\mathcal{A}\nabla w\}\cdot[v] + \{\mathcal{A}\nabla v\}\cdot[w]\, ds + \sum_{F\in\mathcal{F}^{BC}(\zeta)}\int_F\frac{\mathcal{A}\mathcal{D}}{\mathcal{C}}wv\, ds, \end{aligned} \tag{12}$$

and $(\cdot,\cdot)$ denotes the standard linear form. Similarly, the DG approximation for the SP_3 system reads as follows: Find $\phi_h \in V_{\mathbf{p}}(\zeta) \times V_{\mathbf{p}}(\zeta)$ such that

$$B\left(\phi_h, v_h\right) + K_h\left(\phi_h, v_h\right) = \left(\mathcal{F}, v_h\right) + \sum_{F \in \mathcal{F}^{BC}(\zeta)} \int_F \frac{\mathcal{A}}{\mathcal{C}} \mathcal{G} v_h \, ds, \qquad \forall v_h \in V_{\mathbf{p}}(\zeta) \times V_{\mathbf{p}}(\zeta),$$

where B and K_h are defined in (12). Note that in general the penalty parameter in (12) $\gamma > 0$ is chosen large enough so that the operator $B + K_h$ is coercive.

In the presence of steep radiative gradients and boundary layers as those obtained by SP_1 and SP_3 approximations of radiative transfer, the above DG method would need extremely refined meshes to resolve these radiative features. To overcome this difficulty in the present work we consider an anisotropic *hp*-adaptivity using a residual based a posteriori error estimate. Rigorous proofs for the error estimators in the SP_1 and SP_3 equations can be achieved using the same steps as those reported in [11] and therefore are omitted here. Hence, the error estimator for the considered problems is given by

$$\eta_{\text{err}} = \sqrt{\sum_{K \in \zeta} \left(\eta_{R,K}^2 + \eta_{B,K}^2 + \eta_{E,K}^2 + \eta_{J,K}^2 \right)}, \tag{13}$$

where

$$\begin{aligned}
\eta_{R,K}^2 &= \alpha_K^2 \left\| \mathcal{F}_h + \nabla \cdot (\mathcal{A} \nabla \phi_h) - \mathcal{B} \phi_h \right\|_{0,K}^2, \\
\eta_{B,K}^2 &= \sum_{F \in \mathcal{F}^{BC}(K)} \mathcal{A}^{-1/2} \alpha_F \left\| \mathcal{A} \nabla \phi_h \cdot \mathbf{n}_F + \frac{\mathcal{A}\mathcal{D}}{\mathcal{C}} \phi_h - \frac{\mathcal{A}}{\mathcal{C}} \mathcal{G}_h \right\|_{0,F}^2, \\
\eta_{F,K}^2 &= \frac{1}{2} \sum_{F \in \mathcal{F}^{int}(K)} \mathcal{A}_{\min}^{-1/2} \alpha_F \left\| [\mathcal{A} \nabla \phi_h] \right\|_{0,F}^2, \\
\eta_{J,K}^2 &= \frac{1}{2} \sum_{F \in \mathcal{F}^{int}(K)} \left(\frac{\gamma^2 \mathcal{A}_{\max} (p_F^{\perp})^5}{h_{F,K}^{\perp} p_{\min,\mathrm{K}}^2} + \frac{\mathcal{A}_{\max} h_{F,K}^{\perp} p_F^2}{h_{\min,\mathrm{K}}^2} + \frac{\kappa_{\max} h_{F,K}^{\perp}}{p_F^2} + \frac{\mathcal{A}_{\max} h_{F,K}^{\perp} p_{\max,\mathrm{K}}^4}{(p_F^{\perp})^2} \right) \left\| [\phi_h] \right\|_{0,F}^2,
\end{aligned}$$

with $\mathcal{F}_h$ and $\mathcal{G}_h$ are the L^2-projection of $\mathcal{F}$ and $\mathcal{G}$ respectively onto the finite element space. Here, $\mathcal{A}_{\min}$ and $\mathcal{A}_{\max}$ are the matrices constructed taking respectively the minimum and the maximum component by component of the definitions of $\mathcal{A}$ from the two elements sharing a face and

$$\begin{aligned}
\alpha_K &= \min \left(h_{\min,K} \mathcal{A}^{-\frac{1}{2}} p_{\min,K}^{-1}, {\kappa_{\min}}^{-\frac{1}{2}} \right), \\
\alpha_F &= \min \left(h_{\min,K}^2 \left(h_F^{\perp} \right)^{-1} {\mathcal{A}_{\min}}^{-\frac{1}{2}} p_{\min,K}^{-2} p_F^{\perp}, {\kappa_{\min}}^{-\frac{1}{2}} \right),
\end{aligned}$$

where $\kappa_{\min}$ is the minimum value of κ_k on the computational domain Ω, $\|\cdot\|_{0,K}$ and $\|\cdot\|_{0,F}$ are respectively the L^2-norm on an element K and on an face F.

Adopting similar analysis from [11] it is possible to prove that the error estimator is an upper bound for the reference error in the DG norm $|||\cdot|||_{\zeta}$ *i.e.*,

$$|||\phi - \phi_h|||_{\zeta} \leq C \left(\eta_{\text{err}} + \Theta \right),$$

where C is a positive constant independent of the mesh nor the order of the elements used and

$$\Theta = \sqrt{\sum_{K \in \zeta} \frac{h_{\min,K}^2}{\mathcal{A}_{\min} p_K^2} \left\| \mathcal{F} - \mathcal{F}_h \right\|_{0,K}^2 + \sum_{F \in \mathcal{F}^{BC}(\zeta)} \frac{h_{\min,K}^2}{\mathcal{A}_{\min} p_F^2 h_{F,K}^{\perp}} \left\| \mathcal{G} - \mathcal{G}_h \right\|_{0,F}^2},$$

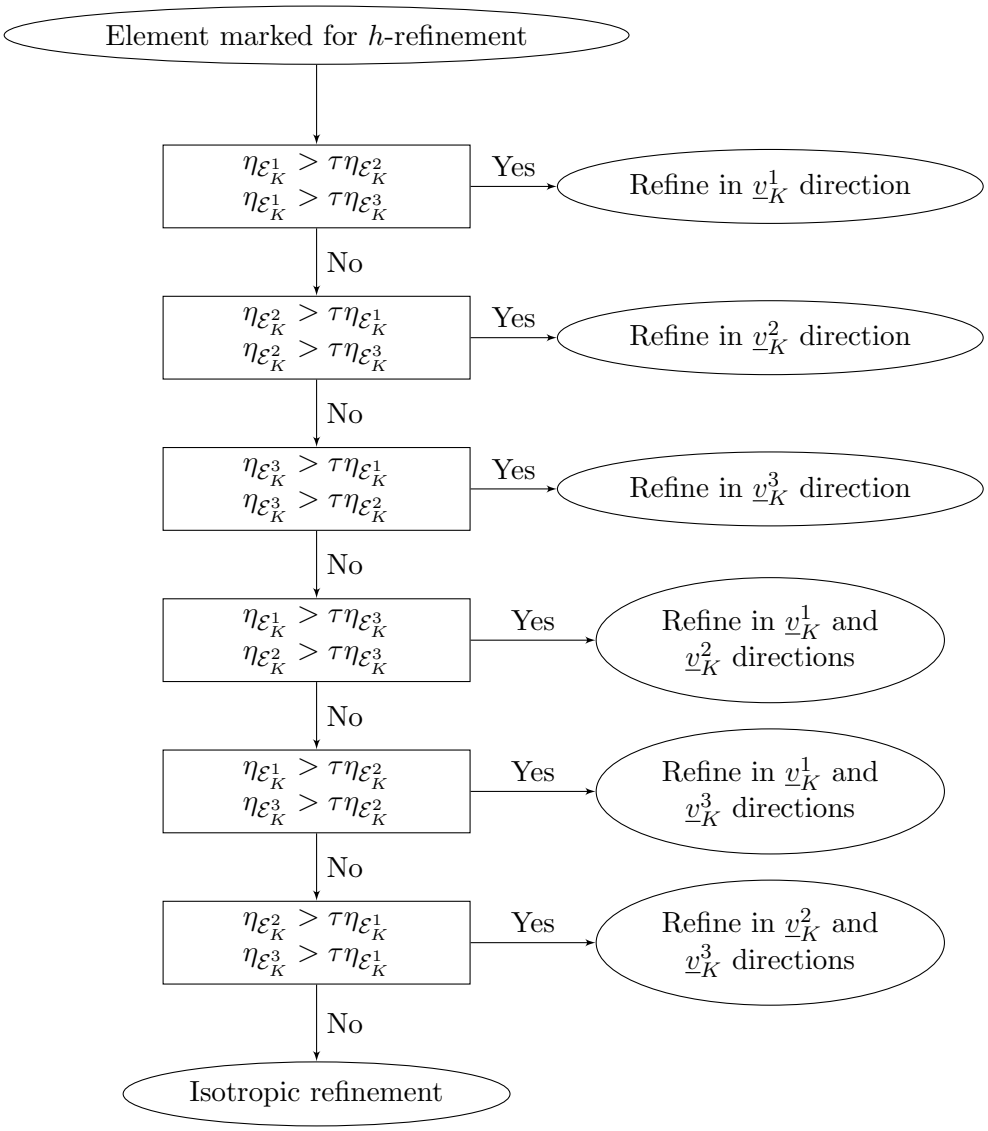

Figure 1: Flowchart of the algorithm used in the present work to apply anisotropic adaptivity.

is the data oscillations. Note that in case of SP_1 and SP_3 equations, the DG norm is defined as

$$|||u|||_\zeta = \left(\sum_{K\in\zeta}\left(\mathcal{A}\left\|\nabla u\right\|^2_{L^2(K)} + \mathcal{B}\left\|u\right\|^2_{0,K}\right) + \sum_{F\in\mathcal{F}^{int}(\zeta)} \frac{\gamma\mathcal{A}(p_F^\perp)^2}{h_F^\perp}\left\|[u]\right\|^2_{0,F} + \sum_{F\in\mathcal{F}^{BC}(\zeta)} \frac{\mathcal{A}\mathcal{D}}{\mathcal{C}}\left\|u\right\|^2_{0,F}\right)^{1/2}.$$

In the present study, numerical implementation of the error estimator η_{err} is carried out using the `AptoFEM`. We consider different adaptive techniques for the SP_1 and SP_3 approximations, namely: isotropic h-adaptivity, isotropic hp-adaptivity, anisotropic h-adaptivity, anisotropic h-adaptivity/isotropic p-adaptivity, anisotropic hp-adaptivity and uniform h-adaptivity. In all our computations, the meshes are adapted by marking the elements for refinement according to the size of the local error indicators (13). This is achieved by employing the fixed fraction strategy proposed in [13], with a refinement fraction of 15%. Thus, for each element $K \in \zeta$ marked for refinement the schemes automatically decide whether the local mesh size h_K or the local polynomial

degree p_K should be adjusted accordingly. The choice to perform either h- or p-refinement is based on estimating the local smoothness of the (unknown) analytical solution. To this end, we employ the hp-adaptive strategy developed in [14], where the local regularity of the analytical solution is estimated from truncated local Legendre expansions of the computed numerical solution.

Notice that if anisotropic h-refinement or anisotropic p-refinement is considered in the scheme, one needs to chose the directions of the anisotropic refinement. In order to make this choice we denote by $\mathcal{E}_K^1$, $\mathcal{E}_K^2$ and $\mathcal{E}_K^3$ the three sets containing opposite faces of the element K, and we define

$$\eta_{\mathcal{E}_K^i} = \sqrt{\eta_{E,K}^2\Big|_{\mathcal{E}_K^i} + \eta_{B,K}^2\Big|_{\mathcal{E}_K^i} + \eta_{J,K}^2\Big|_{\mathcal{E}_K^i}}, \qquad i = 1, 2, 3.$$

Then the choice between isotropic refinement or anisotropic refinement is made comparing the error quantities $\eta_{\mathcal{E}_K^i}$ $(i = 1, 2, 3)$ as in Figure 1 for a parameter $\tau > 1$. The same algorithm is used for elements marked for either anisotropic h-refinement or anisotropic p-refinement, so once the directions of refinement are found, either h or p refinement is applied on only those directions depending on the test of the local smoothness. In all the simulations presented in the current study we used $\tau = 10$ which seems to deliver a good balance between anisotropic and isotropic refinements.

4 Numerical results

In this section we examine the performance of our multi-hp adaptive DG method for several test problems in 3D radiative transfer. Numerical results are presented for both gray and non-gray media using different values for the optical scale ε. Here, the temperature of the media $T(x, y, z)$ is assumed to be known inside the domain Ω and it is fixed to the surrounding temperature $T_b(x, y, z)$ on the domain boundary $\partial\Omega$. This temperature variation between the media and the surrounding generates thermal boundary layers the steepness of which depends on the thermal properties of the media. For small values of ε very sharp boundary layers are expected to be detected in the domain boundary. Most of conventional finite element methods fail to accurately capture these features unless a heavily refined mesh is used in their simulations. In the sequel, we shall use the terminology iso$h$, isohp, aniso$h$, aniso$h$iso$p$, anisohp and unif$h$ to refer to the DG method using, isotropic h-adaptivity, isotropic hp-adaptivity, anisotropic h-adaptivity, anisotropic h-adaptivity/isotropic p-adaptivity, anisotropic hp-adaptivity and uniform adaptivity, respectively. It should be pointed out that we do not consider the strategy isotropic h-adaptivity/anisotropic p-adaptivity because in general the anisotropic p-adaptivity improves the results the most when used with anisotropic h-adaptivity. In all our simulations presented in this section, the resulting linear systems of algebraic equations are solved using the GMRES solver with ILU in PETSc. All the computations are performed on an Intel® Core i7 PC with 16 GB of RAM and 3.60 GHz. The codes only take the default optimization of the machine, *i.e.* they are not parallel codes.

4.1 Accuracy test problems

Our first set of test examples consist of assessing the accuracy of the multi-hp adaptive DG method for problem with known exact solutions as those studied for 2D problems in [12]. First, we solve the SP_1 problem in a gray unit cube $\Omega = [0, 1] \times [0, 1] \times [0, 1]$ using $\sigma = \kappa = 1$ and $r_1 = r_2 = 0$. The functions $\mathcal{F}$ and $\mathcal{G}$ in the right-hand side of SP_1 equations (10) are calculated such that the analytical solution of the SP_1 problem is given by

$$\varphi(x, y, z) = \left(\frac{e^{\frac{x-1}{\mathcal{A}}} - 1}{e^{-\frac{1}{\mathcal{A}}} - 1} + x - 1\right)\left(\frac{e^{\frac{y-1}{\mathcal{A}}} - 1}{e^{-\frac{1}{\mathcal{A}}} - 1} + y - 1\right).$$

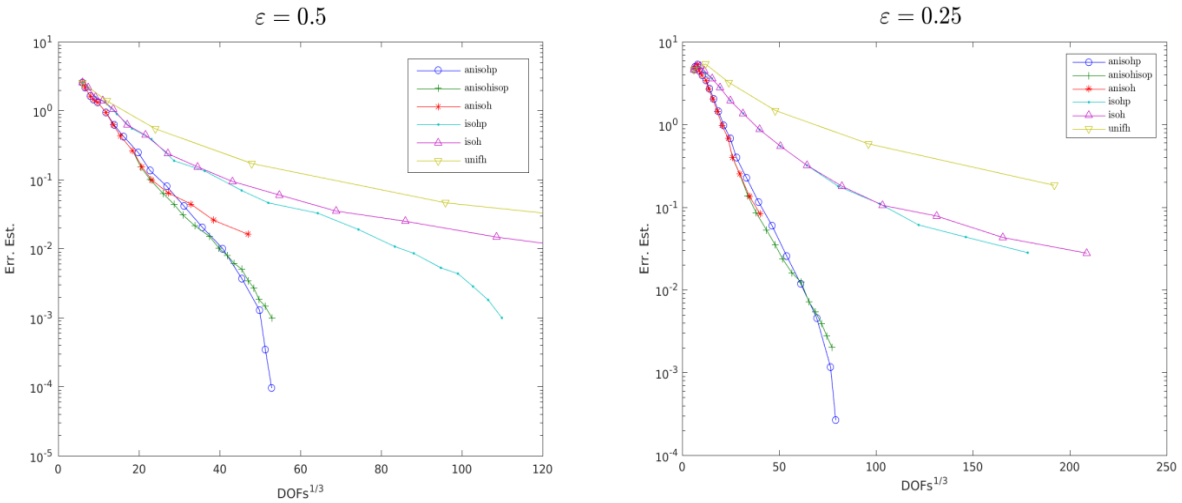

Figure 2: Convergence results in the DG norm using different refinement techniques for the accuracy test problem of the SP_1 model with known exact solution using $\varepsilon = 0.5$ (left) and $\varepsilon = 0.25$ (right).

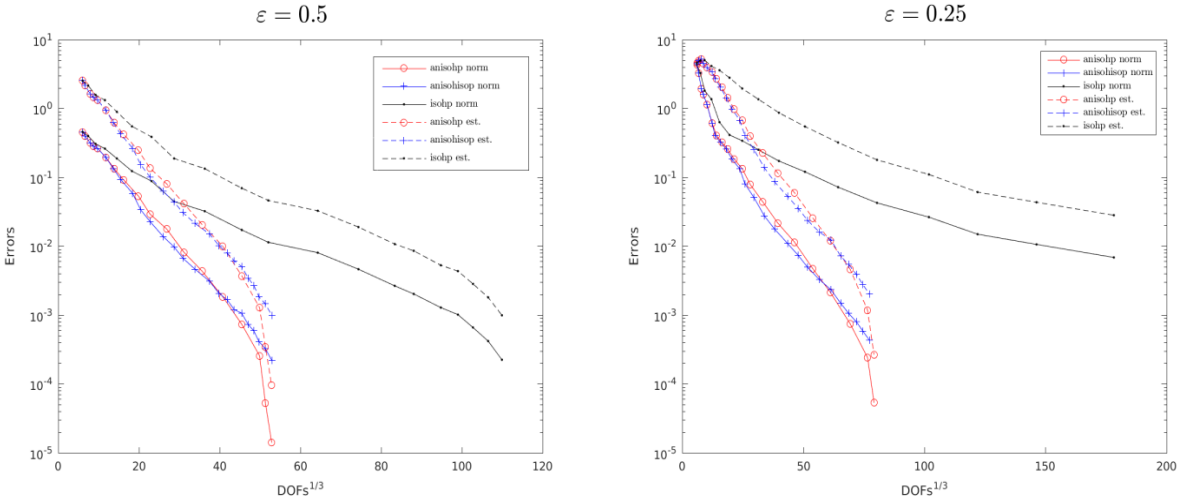

Figure 3: Comparison between the DG norm of the error and the error estimator for the accuracy test problem of the SP_1 model with known exact solution using $\varepsilon = 0.5$ (left) and $\varepsilon = 0.25$ (right).

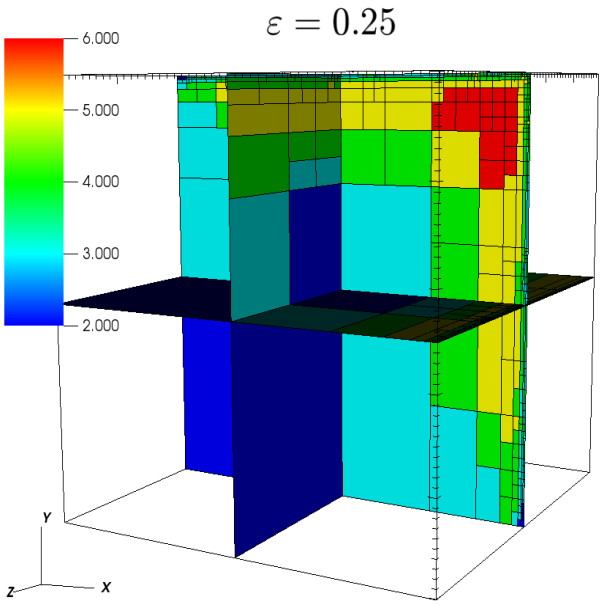

Figure 4: Adapted mesh using anisotropic h-refinement and isotropic p-refinement for the accuracy test problem of the SP_1 model with known exact solution using $\varepsilon = 0.25$. Colors in the mesh indicate the order of polynomials used in each element.

We consider two different values of the diffusion scale namely, $\varepsilon = 0.5$ and $\varepsilon = 0.25$. These values of ε develop boundary layers on the domain boundary $\partial\Omega$ and sharper boundary layers are expected for smaller values of ε.

In Figure 2 we present the convergence of the errors using different refinement techniques for both values of ε. It is clear that there is a huge difference between the adaptive techniques that involve some kind of anisotropic refinement, either in h or p or in both, and the others that use only isotropic refinement. The formers exhibit smaller errors compared to the others for the selected values of ε. However, when the convergence rate is considered, two different classes appear, the first for the techniques that use p-refinement and the other for the remaining techniques that involve only h-refinement. In this respect, the methods in the first class converge exponentially whereas the others only polynomially. It should also be stressed that, due to the existence of the boundary layers in this example, the use of the anisotropic refinement seems to be advantageous for the DG method. It is also interesting to notice that for $\varepsilon = 0.25$, the boundary layers are stronger than the case with $\varepsilon = 0.5$ and the adaptive techniques which do not use anisotropic adaptivity have more difficulties to reduce the error. On the other hand, using anisotropic adaptivity the convergence is much faster and it occurs much sooner than other adaptive procedures. For the considered diffusion scales, the anisohp adaptivity achieves the fastest convergence for this test example compared to other adaptive techniques.

In order to check the behavior of the error estimator and how well it follows the true error, we illustrate in Figure 3 the three hp-adaptivity techniques from Figure 2 namely, anisohp, aniso$h$iso$p$ and isohp procedures along with the computed values of the estimator η_{err}. It is clear that the error estimator η_{err} follows very well the decay of the error in all cases which proves that it is a good estimation of the error. For both considered values of ε, the error estimator η_{err} is always an upper bound for the true error. Notice that the gap between the true value of the error and

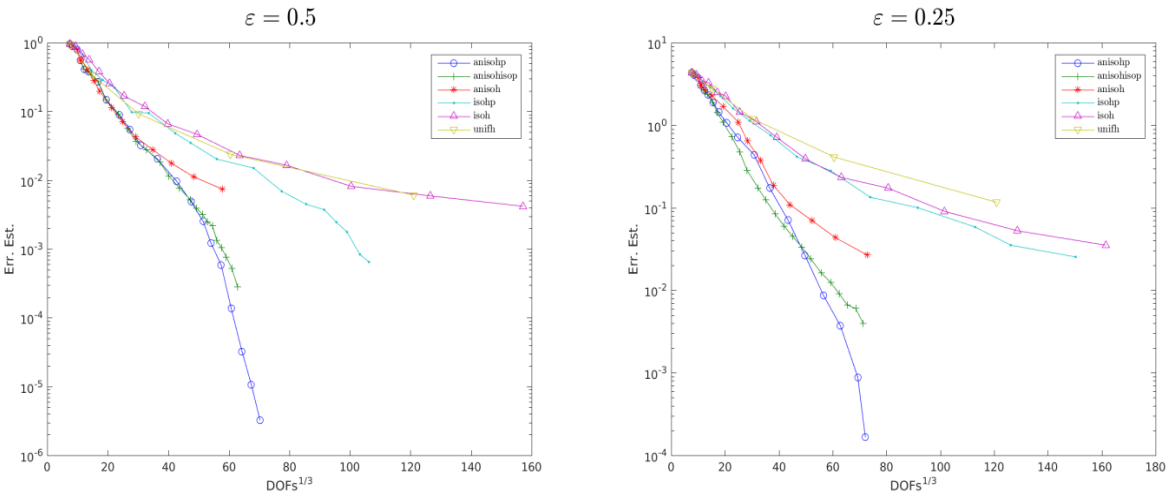

Figure 5: Convergence results in the DG norm using different refinement techniques for the accuracy test problem of the SP_3 model with known exact solution using $\varepsilon = 0.5$ (left) and $\varepsilon = 0.25$ (right).

the error estimator is normal for this kind of error estimators as already analyzed in [11]. Figure 4 depicts the final adapted mesh using aniso*h*iso*p* procedure for the case with $\varepsilon = 0.25$. Recall that the initial mesh was consisting of only eight elements and with polynomial degrees two. Note that the colors in the adapted mesh indicate the order of polynomials used in each element. As it can be seen from these results, the boundary layers have been accurately detected and treated using the anisotropic h-refinement as expected and accordingly to their strength.

Our second accuracy test example consists of solving the SP_3 equations with known analytical solutions. Here, we solve the equations (10) on the unit cube using $\sigma = \kappa = 1$, $\alpha_1 = \alpha_2 = \beta_1 = \beta_2 = 1$ and $\mu_1 = \mu_2 = 1$. The right-hand side $\mathcal{F}$ and the boundary function $\mathcal{G}$ in equations (10) are analytically evaluated such that the exact solution of the SP_3 model is

$$\begin{aligned}
\psi_1(x,y,z) &= \left(\frac{e^{\frac{-x}{\mathcal{A}}}-1}{e^{-\frac{1}{\mathcal{A}}}-1} - x\right)\left(\frac{e^{\frac{-y}{\mathcal{A}}}-1}{e^{-\frac{1}{\mathcal{A}}}-1} - y\right), \\
\psi_2(x,y,z) &= \left(\frac{e^{\frac{x-1}{\mathcal{A}}}-1}{e^{-\frac{1}{\mathcal{A}}}-1} + x - 1\right)\left(\frac{e^{\frac{y-1}{\mathcal{A}}}-1}{e^{-\frac{1}{\mathcal{A}}}-1} + y - 1\right).
\end{aligned}$$

Note that for this test example, the solution components ψ_1 and ψ_2 present boundary layers in the upper-right and lower-left regions of the computational domain, respectively. This problem is well-suited to test if the indicator η_{err} is able to pick up the steep gradients near these boundaries using anisotropic refinements. As in the previous test problem, we consider the two radiative regimes associated with $\varepsilon = 0.5$ and $\varepsilon = 0.25$.

Figure 5 presents the convergence results in the DG norm using different refinement techniques for $\varepsilon = 0.5$ and $\varepsilon = 0.25$. Comparison between the DG norm of the error and the error estimator using the selected values of ε is depicted in Figure 6. The same conclusions on the different adaptive techniques can be drawn for the SP_3 model as for the SP_1 model in terms of convergence rates and magnitude of the errors. The fact that the SP_3 model is a system of two equations, does not seem to affect the quality of the results in our DG method. It is worth pointing out that the boundary layers for this test example are adapted similarly to those reported in Figure 4 for the SP_1 equations and, for brevity in presentation, are not presented here. Again, the anisotropic h-refinement resolves the SP_3 equations very well and it correctly captures the boundary layers in their solutions.

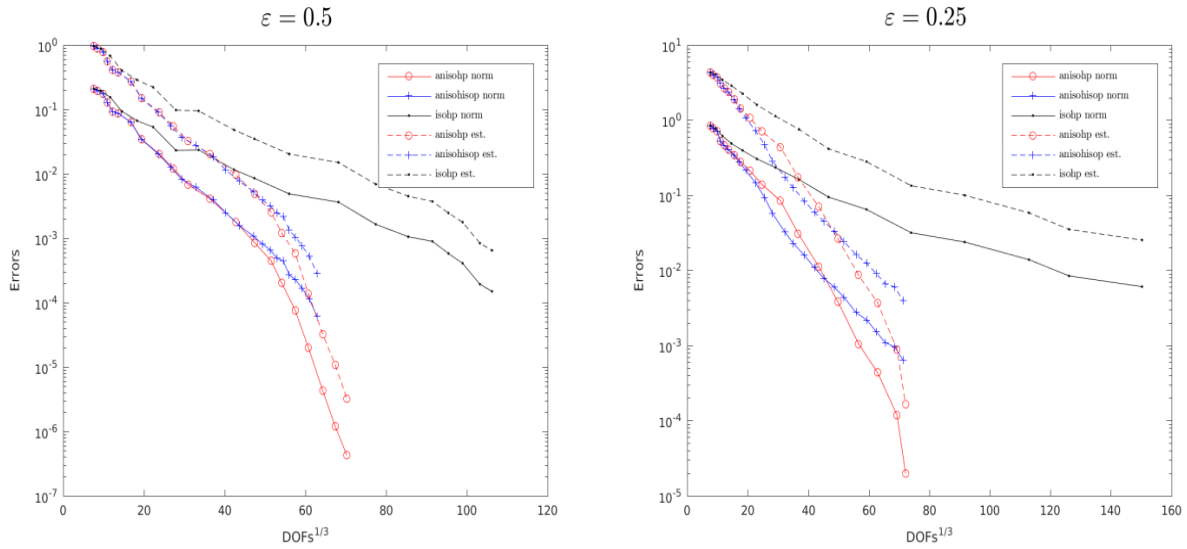

Figure 6: Comparison between the DG norm of the error and the error estimator for the accuracy test problem of the SP_3 model with known exact solution using $\varepsilon = 0.5$ (left) and $\varepsilon = 0.25$ (right).

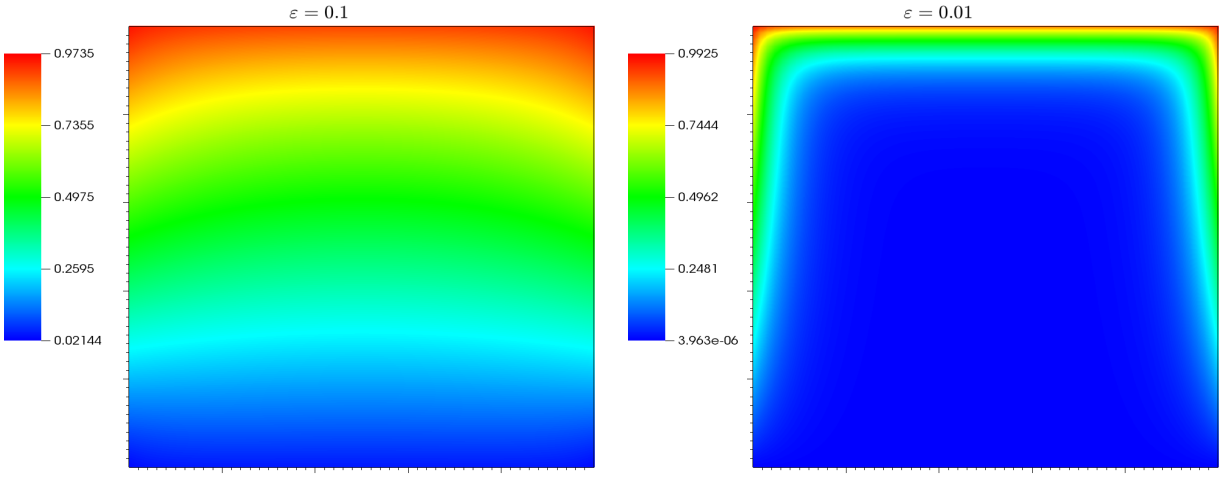

Figure 7: Mean radiative intensity in the xz-plane at $y = 0.5$ obtained for the SP_1 approximation of the first verification example using $\varepsilon = 0.1$ (left column) and $\varepsilon = 0.01$ (right column).

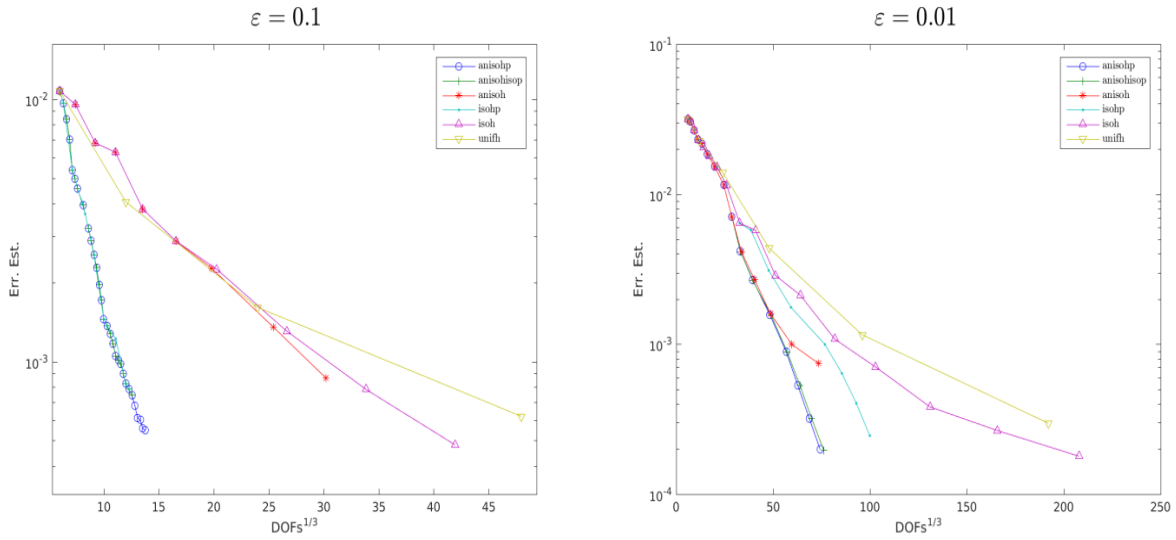

Figure 8: Convergence results in the DG norm using different refinement techniques for the SP_1 approximation of the first verification example using $\varepsilon = 0.1$ (left column) and $\varepsilon = 0.01$ (right column).

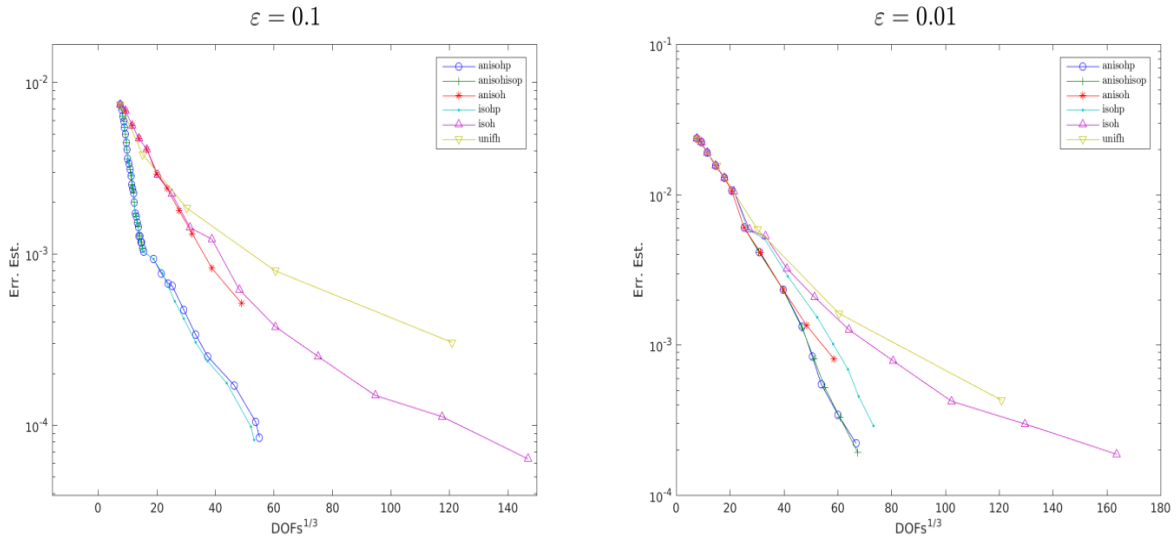

Figure 9: Same as Figure 8 but for the SP_3 approximation.

Table 1: Mesh statistics, convergence results and computational times for the SP_1 approximation of the first verification example using $\varepsilon = 0.1$ and $\varepsilon = 0.01$. The CPU times are given in seconds.

	$\varepsilon = 0.1$				$\varepsilon = 0.01$			
Mesh	# Elems	# DoFs	η_{err}	CPU	# Elems	# DoFs	η_{err}	CPU
1	8	216	0.10729E-01	0.05	8	216	0.31620E-01	0.05
2	8	253	0.96407E-02	0.07	15	405	0.30326E-01	0.09
3	8	290	0.83745E-02	0.09	29	783	0.26625E-01	0.18
4	8	327	0.70235E-02	0.10	51	1377	0.23084E-01	0.32
5	8	364	0.53675E-02	0.12	86	2322	0.21591E-01	0.56
6	8	401	0.49870E-02	0.14	150	4050	0.18439E-01	0.95
7	8	438	0.45711E-02	0.16	285	7695	0.15295E-01	1.89
8	8	536	0.39502E-02	0.29	543	14661	0.11539E-01	3.64
9	8	634	0.32252E-02	0.40	873	23571	0.70862E-02	5.95
10	8	695	0.28945E-02	0.49	1316	36142	0.41618E-02	10.09
11	8	756	0.25461E-02	0.58	2207	61095	0.26936E-02	10.98
12	8	817	0.22738E-02	0.67	3742	112597	0.15742E-02	30.62
13	8	878	0.19624E-02	0.76	5703	182686	0.89032E-03	50.71
14	8	939	0.17173E-02	0.86	7313	247623	0.52948E-03	80.76
15	8	1000	0.14522E-02	0.96	8480	324500	0.31823E-03	100.98
16	8	1091	0.13674E-02	1.73	9893	409368	0.19955E-03	300.02
17	8	1182	0.12754E-02	2.37	11384	566966	0.42824E-03	700.07
18	8	1273	0.11683E-02	3.01	12650	707600	0.26412E-03	900.42
19	8	1364	0.10493E-02	3.58	14127	987430	0.17879E-03	2000.27
20	8	1455	0.10093E-02	4.15	15392	1372110	0.14302E-03	5000.95

4.2 Verification test problems

This test example aims to assess the performance of the proposed DG method compared to the full radiative transfer. We consider two test cases for the solution of the SP_1 and SP_3 approximations using $\varepsilon = 0.1$ and $\varepsilon = 0.01$ in a non-reflective gray unit cube $\mathcal{D} = [0,1] \times [0,1] \times [0,1]$ with $\mathcal{F} = 0$ in (10). In the first example, the boundary function $\mathcal{G}$ is defined as

$$\mathcal{G}(x, y, z) = z,$$

and we set the coefficients $\kappa = 0.01$ and $\sigma = 0.99$. In Figure 7 we illustrate the 2D distributions of the mean radiative intensity in the xz-plane at $y = 0.5$ obtained using the SP_1 with $\varepsilon = 0.1$ and $\varepsilon = 0.01$. It is clear that a smaller ε creates stronger boundary layers in the computational domain. Notice that, since for these test examples the analytical solutions are not available, we only present the decay of the error estimator η_{err}. However, as it has been clearly shown in the previous accuracy test problems with known exact solutions, the error estimator mimics very well the behavior of the reference error and it is always an upper bound for this error in all optical regimes considered. This should give us the confidence that also the true error is decaying in a similar way as the error estimator associated with these problems. Hence, Figure 8 presents the convergence results of the error estimator in the DG norm for this test example using different refinement techniques for the SP_1 approximation with $\varepsilon = 0.1$ and $\varepsilon = 0.01$. Those results obtained for the SP_3 approximation for this example are presented in Figure 9. The corresponding mesh statistics and CPU times for the considered problem using anisohp-adaptivity are summarized in Table 1 for both diffusion scales. Here, the listed CPU time includes the computational time used to assemble the system, to solve this system and to compute the error estimator. It is clear that for this test example more degrees of freedom are needed for simulations using $\varepsilon = 0.01$ than those using $\varepsilon = 0.1$. Similar trends have been observed for results, not reported here, using the SP_3 approximation for this test example.

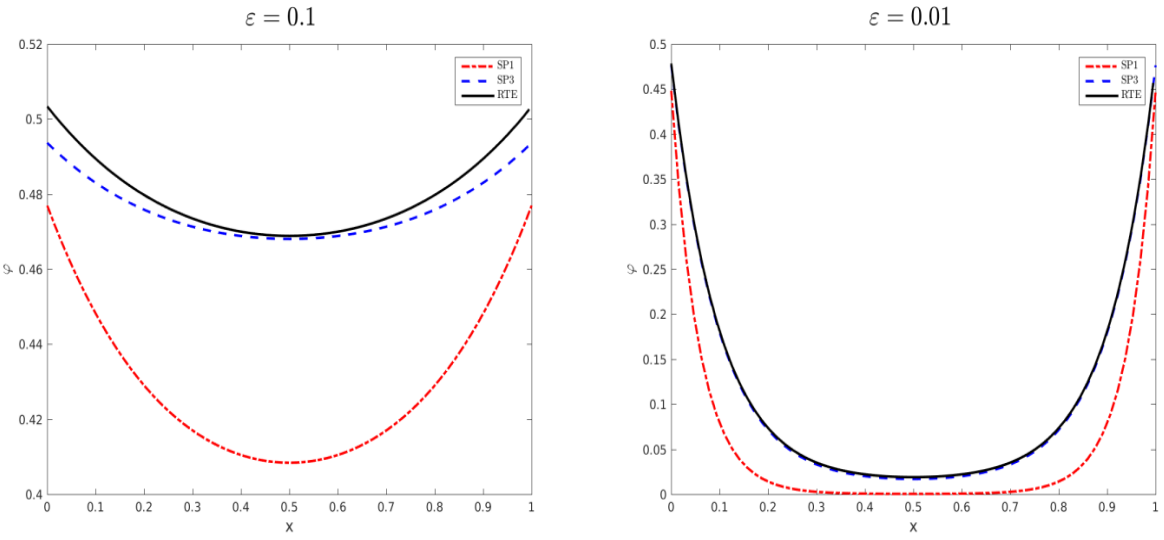

Figure 10: Comparison between the results obtained using the SP_1 and SP_3 models to those obtained using the full RTE for the first verification example using $\varepsilon = 0.1$ (left) and $\varepsilon = 0.01$ (right).

Next we compare the results obtained using the DG method for the SP_1 and SP_3 models to those obtained using a direct solver for the full radiative transfer equations (1)-(3). Here, as a direct solver for the RTE we consider the well-established Diffusion Synthetic Acceleration (DSA) method. This method uses the diffusion approach to accelerate the source iteration which has been widely used in computational radiative transfer. We refer to [22, 21] for the implementation of the DSA method and further discussions on other direct methods can also be found therein. We use the S_8 discrete-ordinate algorithm for the discretization of the angle variable and a mesh of $200 \times 200 \times 200$ nodes for $\varepsilon = 0.1$ and $400 \times 400 \times 400$ nodes for $\varepsilon = 0.01$ are used in our computations. These angle and mesh discretizations yield linear systems with 64×10^7 and 512×10^7 unknowns which has to be solved for the case with $\varepsilon = 0.1$ and $\varepsilon = 0.01$, respectively. These numbers of unknowns are associated with the SP_1 model and they should be doubled in the case of the SP_3 model. Figure 10 exhibits the 1D cross-sections at centerline with $y = z = 0.5$ of the mean intensity φ obtained using the SP_1 and SP_3 approximations and the RTE using $\varepsilon = 0.1$ and $\varepsilon = 0.01$. It is clear that for the considered optical regimes, the proposed DG method for SP_1 and SP_3 approximations accurately captures the radiative features of the mean intensity. For instance, the boundary layers in the mean intensity obtained for the SP_3 model using $\varepsilon = 0.01$ are correctly resolved by our DG method and they compare well with those obtained using the DSA solver for the full RTE. It is also evident that, for this test example, the SP_1 and SP_3 models asymptotically resolves the radiative transfer equation as the DSA method does, but with very less computational effort referring to the CPU times. Here, for a tolerance of 10^{-6} and using $\varepsilon = 0.01$, the DSA method needs 793 and 1275 iterations to converge for $\varepsilon = 0.1$ and $\varepsilon = 0.01$, respectively. However, the DG method for the SP_3 model shows fast convergence with a CPU time about 980 times lower than the DSA method for the same simulations.

As a second verification example we solve the SP_1 and SP_3 approximations in a non-reflective

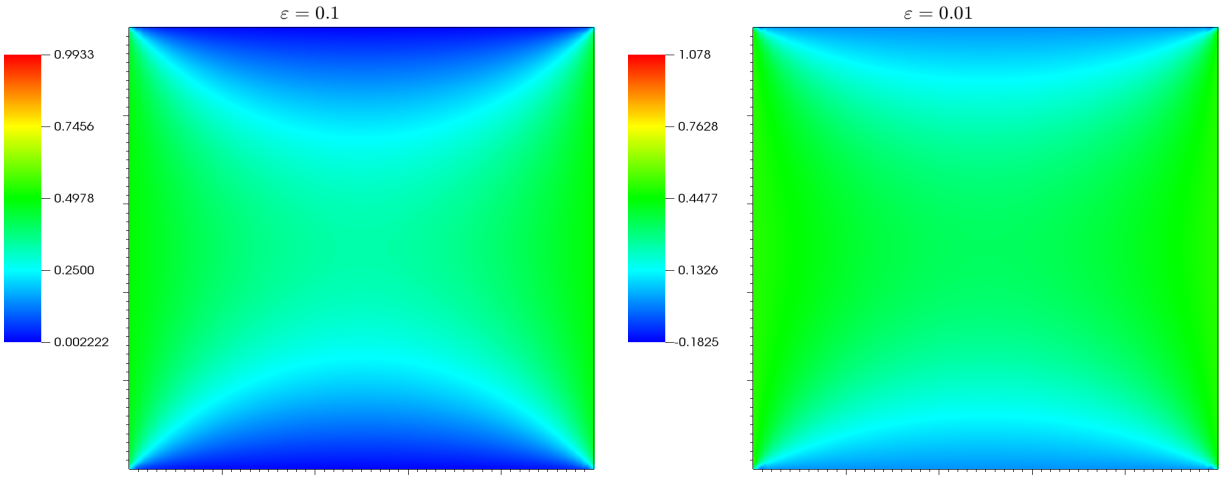

Figure 11: Mean radiative intensity in the xz-plane at $y = 0.5$ obtained for the SP_1 approximation of the second verification example using $\varepsilon = 0.1$ (left column) and $\varepsilon = 0.01$ (right column).

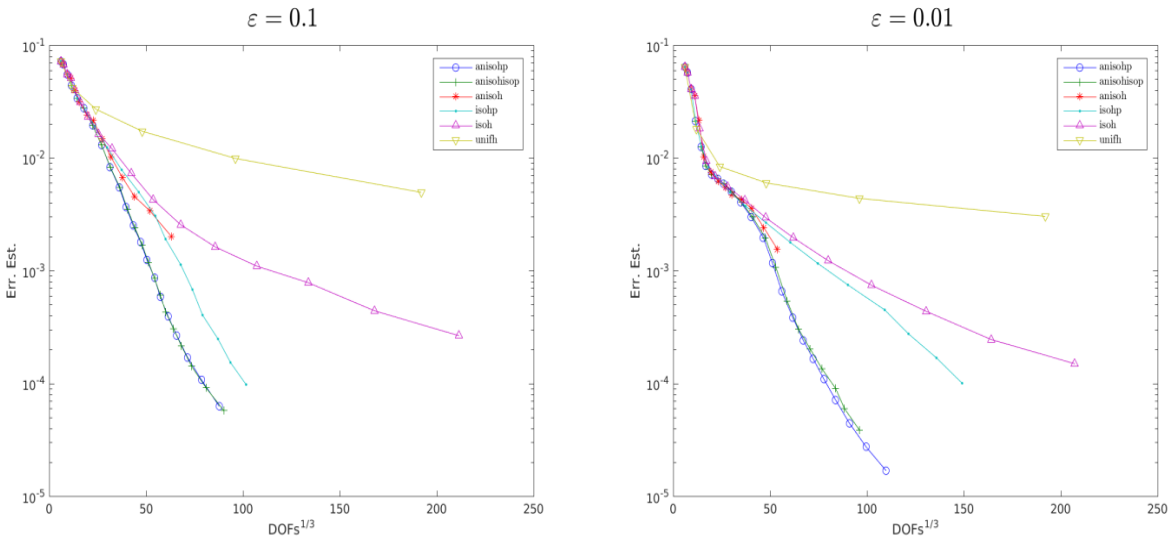

Figure 12: Convergence results in the DG norm using different refinement techniques for the SP_1 approximation of the second verification example using $\varepsilon = 0.1$ (left column) and $\varepsilon = 0.01$ (right column).

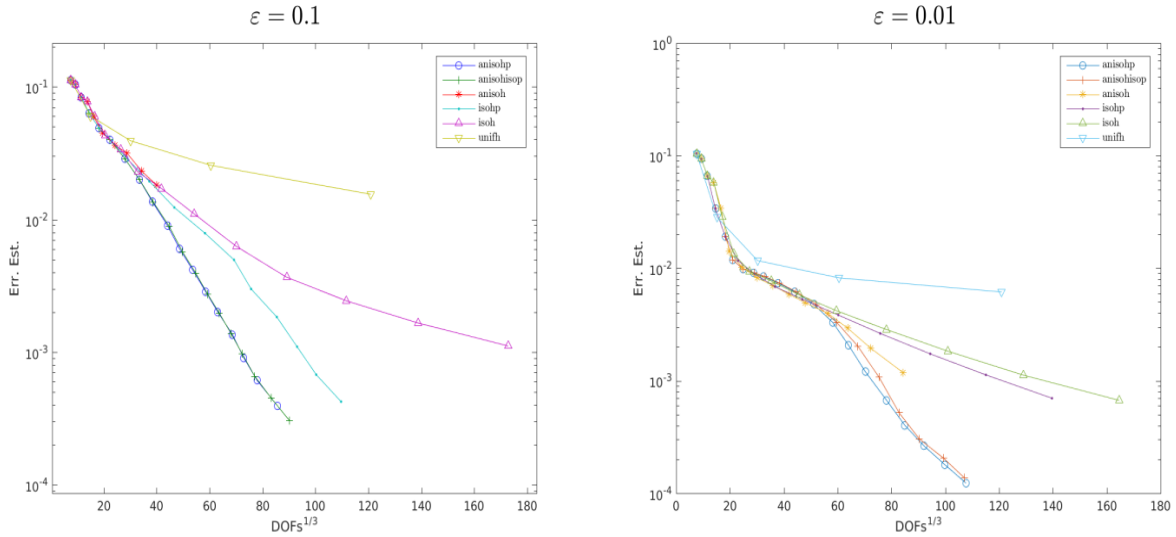

Figure 13: Same as Figure 12 but for the SP_3 approximation.

Table 2: Mesh statistics, convergence results and computational times for the SP_1 approximation of the second verification example using $\varepsilon = 0.1$ and $\varepsilon = 0.01$. The CPU times are given in seconds.

	$\varepsilon = 0.1$				$\varepsilon = 0.01$			
Mesh	# Elems	# DoFs	η_{err}	CPU	# Elems	# DoFs	η_{err}	CPU
1	8	432	0.74151E-02	0.10	8	432	0.23531E-01	0.10
2	8	506	0.69127E-02	0.17	15	810	0.22258E-01	0.22
3	8	580	0.63530E-02	0.22	29	1566	0.18922E-01	0.44
4	8	654	0.59168E-02	0.28	57	3078	0.15549E-01	0.90
5	8	728	0.54645E-02	0.34	106	5724	0.12875E-01	1.78
6	8	802	0.49870E-02	0.40	163	8802	0.10548E-01	2.69
7	8	876	0.44551E-02	0.47	297	16038	0.60190E-02	5.03
8	8	950	0.40376E-02	0.53	533	29300	0.41433E-02	10.15
9	8	1024	0.35862E-02	0.62	1126	62970	0.23296E-02	20.67
10	8	1146	0.33609E-02	0.95	1693	102316	0.13181E-02	50.76
11	8	1268	0.31168E-02	0.12	1817	29334	0.83543E-03	100.44
12	8	390	0.28442E-02	1.57	2087	156590	0.54576E-03	100.80
13	8	1512	0.25414E-02	1.90	2230	217520	0.34296E-03	400.95
14	8	1634	0.23885E-02	2.26	2320	298282	0.22144E-03	400.99
15	8	1756	0.22485E-02	2.65	2484	436728	0.16002E-03	1000.35
16	8	1878	0.19936E-02	3.03	2498	485866	0.12223E-03	4000.51

gray unit cube $\mathcal{D} = [0,1] \times [0,1] \times [0,1]$ with $\mathcal{F} = 0$ in (10) and $\mathcal{G}$ defined by

$$\mathcal{G}(x,y,z) = \begin{cases} 1-y, & \text{if} \quad x = 1, \\ y, & \text{if} \quad x = 0, \\ 1-x, & \text{if} \quad y = 1, \\ x, & \text{if} \quad y = 0, \\ 0, & \text{otherwise}, \end{cases}$$

and we set the coefficients $\kappa = 0$ and $\sigma = 10$. As in the previous test example, we display in Figure 11 the 2D distributions of the mean radiative intensity in the xz-plane at $y = 0.5$ for the SP_1 approximation using $\varepsilon = 0.1$ and $\varepsilon = 0.01$. Steeper boundary layers are also detected for $\varepsilon = 0.01$ than for $\varepsilon = 0.1$ and our DG method accurately captures these boundary layers. The convergence results of the error estimator in the DG norm for this example using different refinement techniques using the SP_1 approximation with $\varepsilon = 0.1$ and $\varepsilon = 0.01$ are depicted in Figure 12. Those results obtained using the SP_3 approximation for this example are presented in Figure 13. Comparing the convergence plots for different refinement strategies, it is clear that in all cases the strategies involving only h-adaptivity are the worse ones. In some cases, the aniso$h$-adaptivity performs quite well at the beginning to only slow down later on compared to the strategies involving both h-adaptivity and p-adaptivity. Also for $\varepsilon = 0.1$, the three hp-strategies seem to perform very similar for both SP_1 and SP_3 approximations. However, for $\varepsilon = 0.01$, it is clear that anisohp and aniso$h$-iso$p$ are better than isohp. The reason lies in the fact that for smaller values of ε the boundary layers are stronger and so the possibility to exploit anisotropic$h$-adaptivity is advantageous.

In Table 2 we summarize the mesh statistics and CPU times for the SP_1 approximation of this verification example. As for the first test example, for a fixed accuracy, more degrees of freedom are used for the DG simulations using $\varepsilon = 0.01$ than those using $\varepsilon = 0.1$. This behavior has also been detected in the SP_3 results, not included here for brevity. To further emphasis the performance of our DG method for this test example we display in Figure 14 the final mesh using anisotropic hp-refinement. As it can be seen the boundary layers along the edges have been recognized and refined accordingly.

4.3 Problems with discontinuous variables

In this test example we examine the performance of our DG method for solving the SP_N approximations with discontinuous variables. For brevity in the presentation we only consider the SP_1 model for this example. Here, we solve the SP_1 equations (8) in a gray unit cube $\mathcal{D} = [0,1] \times [0,1] \times [0,1]$ subject to discontinuous temperature distribution, scattering and absorption coefficients. Note that for a gray media the Planck function (2) reduces to

$$B(T) = a_R T^4,$$

where $a_R = 5.67 \times 10^{-8}$ is the reduced Boltzmann constant [17]. The temperature distribution, scattering and absorption coefficients are discontinuous and defined as

$$T(x,y,z) = \begin{cases} 550\ K, & \text{if} \quad (x,y,z) \in \Omega_1, \\ 500\ K, & \text{elsewhere}, \end{cases}$$

$$\sigma(x,y,z) = \begin{cases} 1 & \text{if} \quad (x,y,z) \in \Omega_1, \\ 0, & \text{elsewhere}, \end{cases} \qquad \kappa(x,y,z) = \begin{cases} 1 & \text{if} \quad (x,y,z) \in \Omega_1, \\ 10, & \text{elsewhere}, \end{cases}$$

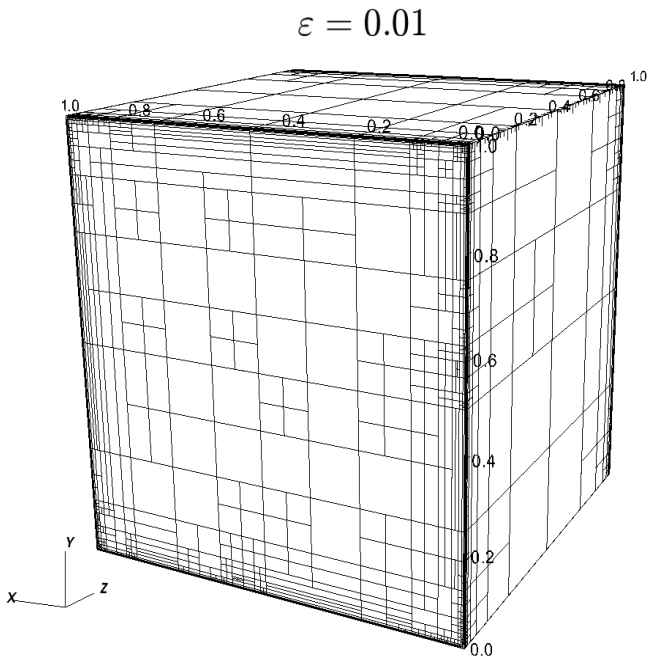

Figure 14: Adapted mesh using anisotropic *hp*-refinement for the SP_1 approximation of the second verification example using $\varepsilon = 0.01$.

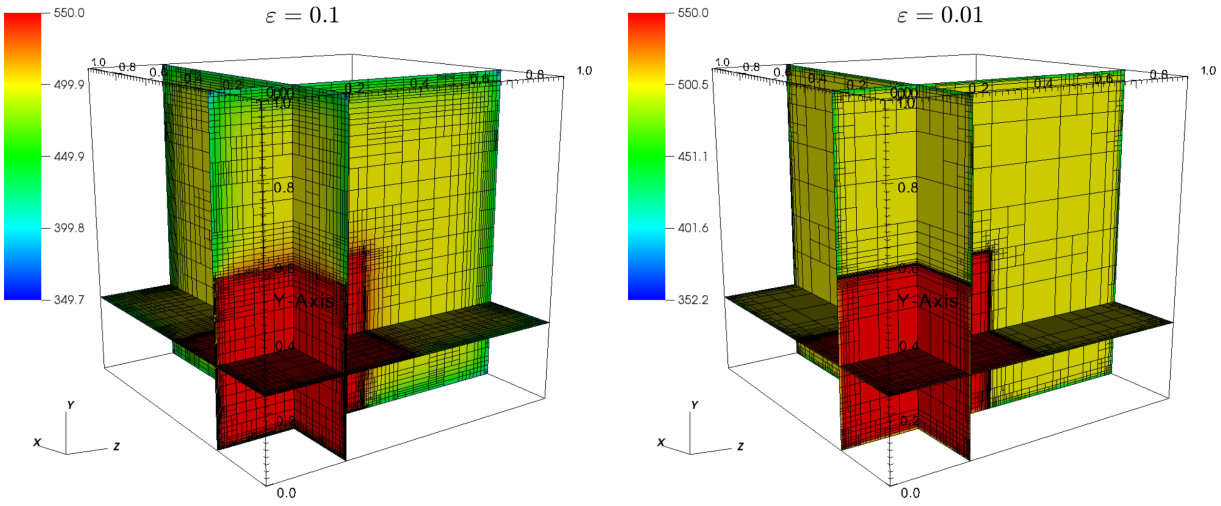

Figure 15: Adapted meshes and the associated radiative temperatures obtained for the SP_1 approximation using $\varepsilon = 0.1$ (left) and $\varepsilon = 0.01$ (right) for the problem with discontinuous variables.

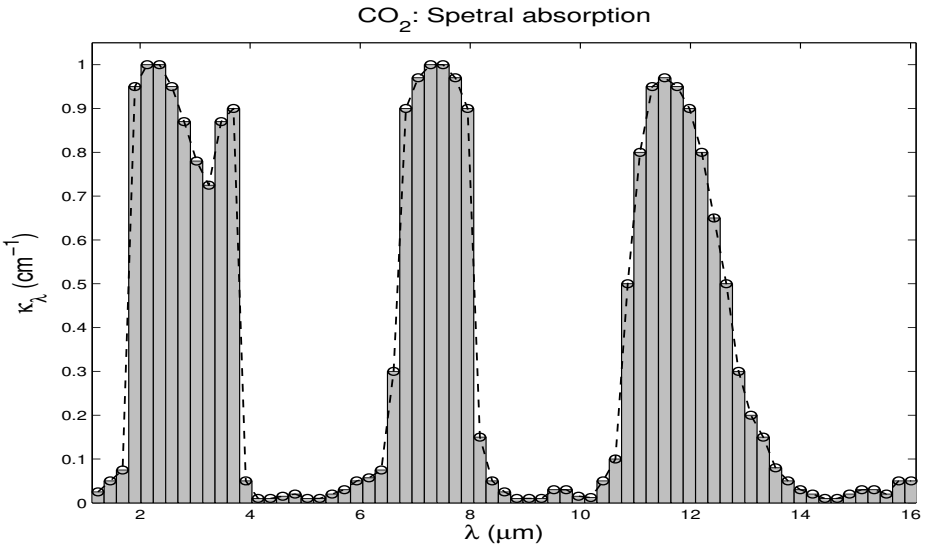

Figure 16: Spectral absorption coefficients used in this study for the species CO_2.

where the sub-domain $\Omega_1 = \left[0, \frac{1}{2}\right] \times \left[0, \frac{1}{2}\right] \times \left[0, \frac{1}{2}\right]$. On the domain boundaries the ambient temperature is set to $T_b = 300\ K$. Due to the discontinuities in the temperature, scattering and absorption coefficients, localized internal and external boundary layers are expected to appear in the solution of this test example. In Figure 15 we display the obtained mean radiative temperature using the SP_1 approximation with $\varepsilon = 0.1$ and $\varepsilon = 0.01$. For better insight only lateral and vertical cross-sections are shown in this figure. We also include the adapted meshes within the results in Figure 15. As expected steeper interface layers are present in the results obtained using $\varepsilon = 0.01$ compared to those obtained using $\varepsilon = 0.1$. From the results shown in Figure 15, our DG method has automatically detected these internal boundary layers and the meshes have been adapted consequently.

4.4 Non-gray radiative transfer problems

Our final example consists of solving the SP_1 and SP_3 approximations for non-gray radiative transfer in combustion problems. In most combustion systems, the CO_2 is one of the dominant radiating species and at high temperatures radiative transfer can not be neglected. In this example, we check the performance of our *hp*-adaptive DG method for solving non-gray SP_1 and SP_3 models. Hence, we solve the non-gray SP_1 equations (8) and the non-gray SP_3 equations (9) in a unit cube $\mathcal{D} = [0,1] \times [0,1] \times [0,1]$ with the CO_2 species. On the domain boundary the temperature is maintained at the ambient temperature of $T_b = 300\ K$ and the interior medium has a steady temperature exponentially decaying from 2500 K to 2000 K as

$$T(x,y,z) = 2000 + 500 \exp\left(-\frac{\sqrt{x^2+y^2+z^2}}{0.08}\right)$$

In Figure 16 we present the spectrum used in our computations for the CO_2 species [6]. The non-opaque frequency interval $[\nu_0, \infty)$ is approximated by 67 bands with piecewise constant absorption coefficients. Since the data are originally defined for the wavelength intervals $[\lambda_{k-1}, \lambda_k]$, we computed the corresponding frequency bands using the relation

$$\nu_k = \frac{c_0}{\lambda_k\, n_m}, \qquad k = 1, 2, \ldots, 67,$$

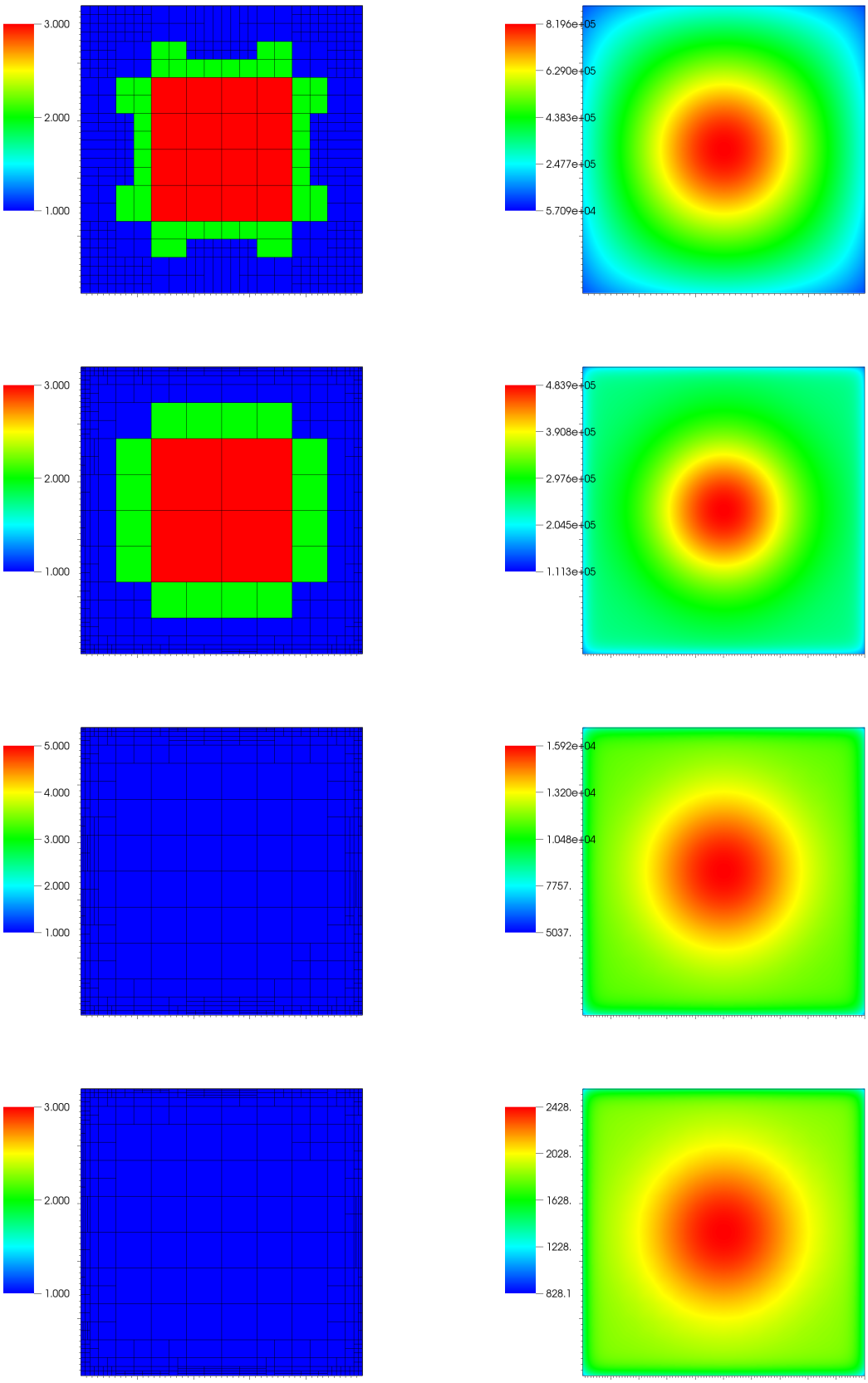

Figure 17: Adapted meshes (left column) and mean radiative intensity (right column) obtained for different frequency bands using SP_1 approximation of the non-gray radiative transfer problem.

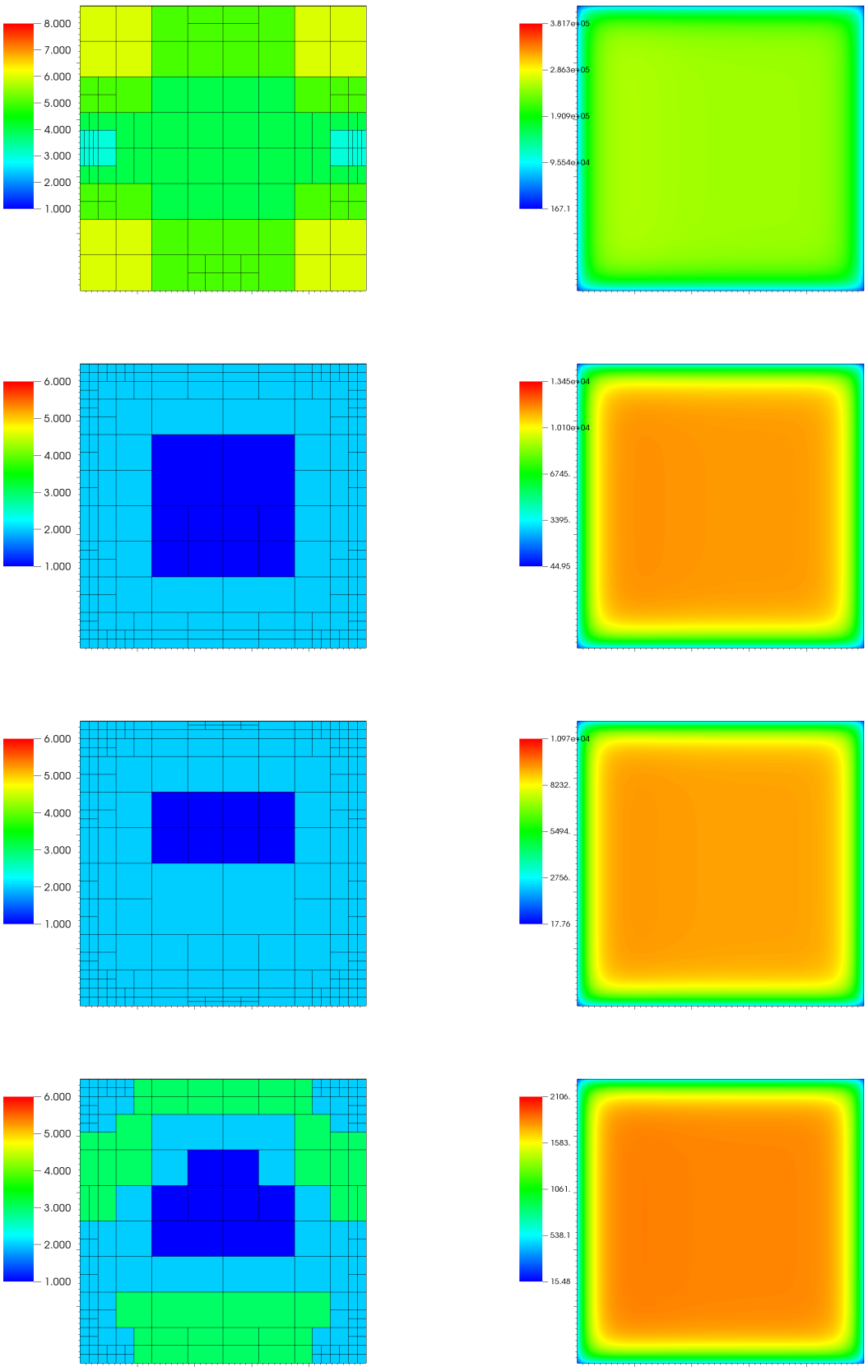

Figure 18: Adapted meshes (left column) and mean radiative intensity (right column) obtained for different frequency bands using SP_3 approximation of the non-gray radiative transfer problem.

Table 3: Number of degrees of freedom of the adapted meshes necessary to reduce the error estimator by 10 times for the four selected frequency bands.

Band	# DoFs in SP_1	# DoFs in SP_3
1	2394	39030
6	10571	48596
27	14268	47346
48	14395	47288

where c_0 is the speed of the light in vacuum. It is evident from this figure that the material is non-gray and the optical properties strongly change with the wavelength. In addition the CO_2 species are considered to be non-scattering and opaque to radiation for wavelengths larger than a cut-off wavelength equal to 16 μm. In all the computations reported herein, we used $c_0 = 2.9979 \times 10^8\ m/s$, $h_P = 6.62608 \times 10^{-34}\ Js$, $k_B = 1.38066 \times 10^{-23}\ J/K$, $n_m = 1.33$ and $\varepsilon = 0.1$. In this study we highlight the effect of an instantaneous change in the ambient temperature from 2000 K to 300 K, causing a sharp drop in the temperature across a boundary layer that can be very thin depending on the physical properties of the enclosure. As a thinner layer is considered the problem becomes more challenging to solve with the continuous finite element methods or the conventional DG methods without adaptivity.

Figure 17 shows the cross-sections in the xy-plane at $z = 0.5$ of the adaptive meshes and the mean radiative intensity φ for the selected bands 1, 6, 27 and 48 using the SP_1 approximation. The results obtained using the SP_3 approximation are shown in Figure 18. As can be seen from the results presented in these figures, the computed mean intensities φ_k ($k = 1, 6, 27$ and 48) exhibit similar radiative patterns with the highest mean intensity located in center of the domain and it decays exponentially to the ambient radiation. However, the speed of this decay and the thickness of the associated boundary layers differ from a band to another. For instance, faster decay and thicker boundary layer have been observed in the 48th band for φ_{48} compared to other bands in both simulations using the SP_1 and the SP_3 approximations. Our numerical simulations demonstrate that the coupling of mesh adaptation and a posteriori error estimate allows for an economical and accurate DG solution of non-gray radiative transfer problems.

In terms of adapted meshes shown in Figure 17 and Figure 18, it is evident that the aniso*hp*-adaptivity patterns are different for each band. Here, the colors in the adapted mesh refer to the order of polynomials used in each element. It is clear that the proposed estimator locates the error very well and the maximum error is well captured at the boundary of the computational domain. In addition, for the considered radiative conditions, we can observe that the number of degrees of freedom differs from one band to another and the *hp*-adaptivity is automatically switched on only when it is needed for the concerned band independently of the other bands, which confirms the relevance of the adaptation criteria based on our error estimator. Finally, we summarize in Table 3 the number of degrees of freedom used for the adapted meshes in order to reduce the error estimator by 10 times compared to the initial value of the error estimator computed on the initial mesh of 64 elements.

5 Conclusions

We have presented a robust class of fully anisotropic *hp*-adaptive discontinuous Galerkin methods for solving 3D simplified P_N approximations of radiative transfer in non-gray media. The thermal

radiation is approximated by the SP_1 and SP_3 models resulting in a set of elliptic equations independent of directional coordinates and easy to be integrated in existing software packages used in computational radiative transfer. The optical spectrum is discretized into a finite set of frequency bands with piecewise constant scattering and absorption coefficients. Using space error estimators a class of high-order adaptive discontinuous Galerkin are developed. The methods use 3D meshes containing finite elements of different kind (tetrahedral, prism and pyramid elements) and the number of equations and polynomial orders of the approximation varying locally on the finite element edges, faces, and interiors. Both isotropic and anisotropic adaptation can carried out for each band in the optical spectrum. To examine the performance of the proposed techniques we have solved several test problems including an example with discontinuous coefficients. We have also solved a non-gray problem involving the CO_2 species with a total of 67 spectral bands. It has been found that it is possible to estimate the radiative field with a computational cost very significantly lower than solving the equations using the conventional finite element method. In addition, for optically thick media the simplified P_N approximations give results which are close to those computed by the full radiative transfer problem. Future work will concentrate on extending these methods to solve the time-dependent radiative heat transfer in three space dimensions and also coupled radiation and convection in non-gray semitransparent media.

References

[1] Z. Altac and M. Tekkalmaz. Benchmark solutions of radiative transfer equation for three-dimensional rectangular homogeneous media. *Journal of Quantitative Spectroscopy and Radiative Transfer*, 109:587–607, 2008.

[2] Z. Altac and M. Tekkalmaz. Exact solution of radiative transfer equation for three-dimensional rectangular, linearly scattering medium. *Journal of Thermophysics and Heat Transfer*, 25:228–238, 2011.

[3] P.R. Amestoy, A. Guermouche, J.Y. L'Excellent, and S. Pralet. Hybrid scheduling for the parallel solution of linear systems. *Parallel Computing*, 32:136–156, 2006.

[4] D.N. Arnold, F. Brezzi, B. Cockburn, and L.D. Marini. Unified analysis of discontinuous Galerkin methods for elliptic problems. *SINUM*, 39:1749–1779, 2002.

[5] R. Backofen, T. Bilz, A. Ribalta, and A. Voigt. SP_N-approximations of internal radiation in crystal growth of optical materials. *J. Crystal Growth.*, 266:264–270, 2004.

[6] P. Cumber, M. Fairweather, and H. Ledint. Application of wide band radiation models to nonhomogeneous combustion systems. *Int. J. Heat Mass Transfer*, 41:1573–1584, 1998.

[7] W. Fiveland. The selection of discrete ordinate quadrature sets for anisotropic scattering. *ASME HTD. Fundam. Radiat. Heat Transfer.*, 160:89–96, 1991.

[8] M. Frank, M. Seaid, J. Janicka, A. Klar, R. Pinnau, and G. Thömmes. A comparison of approximate models for radiation in gas turbines. *Int. J. Progress in CFD*, 3:191–197, 2004.

[9] E.H. Georgoulis, E. Hall, and P. Houston. Discontinuous Galerkin methods on *hp*-anisotropic meshes I: A priori error analysis. *Int. J. Comput. Sci. Math.*, 1:221–244, 2007.

[10] E.H. Georgoulis, E. Hall, and P. Houston. Discontinuous Galerkin methods on *hp*-anisotropic meshes II: A-posteriori error analysis and adaptivity. *Appl. Numer. Math.*, 59:2179–2194, 2009.

[11] S. Giani, D. Schötzau, and L. Zhu. An a-posteriori error estimate for *hp*-adaptive DG methods for convection–diffusion problems on anisotropically refined meshes. *Computers & Mathematics with Applications*, 67:869–887, 2014.

[12] S. Giani and M. Seaid. hp-adaptive discontinuous Galerkin methods for simplified PN approximations of frequency-dependent radiative transfer. *Computer Methods in Applied Mechanics and Engineering*, 301:52–79, 2016.

[13] P. Houston and E. Süli. Adaptive finite element approximation of hyperbolic problems. *Lect. Notes Comput. Sci. Engrg.*, 25:269–344, 2002.

[14] P. Houston and E. Süli. A note on the design of *hp*-adaptive finite element methods for elliptic partial differential equations. *Computer Methods in Applied Mechanics and Engineering*, 194:229–243, 2005.

[15] E. Larsen, G. Thömmes, A. Klar, M. Seaid, and T. Götz. Simplified P_N approximations to the equations of radiative heat transfer and applications. *J. Comp. Phys.*, 183:652–675, 2002.

[16] D. Levermore. Moment closure hierarchies for kinetic theories. *J. Stat. Phys.*, 83:1021–1065, 1996.

[17] D. Mihalas and B.S. Mihalas. *Foundations of Radiation Hydrodynamics.* Oxford University Press, New York, 1983.

[18] M.F. Modest. *Radiative Heat Transfer.* McGraw-Hill, 1993.

[19] G.C. Pomraning. *The Equations of Radiation Hydrodynamics.* Pregamon press, 1973.

[20] D. Schötzau and L. Zhu. A robust a-posteriori error estimator for discontinuous Galerkin methods for convection-diffusion equations. *Appl. Numer. Math.*, 59:2236–2255, 2009.

[21] M. Seaid, M Frank, A. Klar, R. Pinnau, and G. Thömmes. Efficient numerical methods for radiation in gas turbines. *J. Comp. Applied Math.*, 170:217–239, 2004.

[22] M. Seaid and A. Klar. Efficient preconditioning of linear systems arising from the discretization of radiative transfer equation. *Lect. Notes. Comp. Sci.*, 35:211–236, 2003.

[23] M. Seaid, A. Klar, and R. Pinnau. Numerical solvers for radiation and conduction in high temperature gas flows. *Flow, Turbulence and Combustion.*, 75:173–190, 2005.

[24] Z. Tan. Radiative heat transfer in multidimensional emitting, absorbing, and anisotropic scattering media-mathematical formulation and numerical method. *Journal of Heat Transfer*, 111:1–28, 1989.

[25] I. Teleaga, M. Seaid, I. Gasser, A. Klar, and J. Struckmeier. Radiation models for thermal flows at low mach number. *J. Comp. Phys.*, 215:506–525, 2006.

[26] R. Viskanta and E.E. Anderson. Heat transfer in semitransparent solids. *Advances in Heat Transfer*, 11:317–441, 1975.

[27] L. Zhu, S. Giani, P. Houston, and D. Schötzau. Energy norm a-posteriori error estimation for *hp*-adaptive discontinuous Galerkin methods for elliptic problems in three dimensions. *Math. Models Methods Appl. Sci.*, 21(2):267–306, 2010.